J|A|C|S
ARTICLES
Published on Web 01/05/2007

Photoreversible Multiple Additions of Hydrogen to a Highly Unsaturated Platinum−Rhenium Cluster Complex

Richard D. Adams,*,† Burjor Captain,† Chad Beddie,‡ and Michael B. Hall*,‡

Contribution from the Department of Chemistry and Biochemistry, University of South Carolina, Columbia, South Carolina 29208, and Department of Chemistry, Texas A&M University, College Station, Texas 77843-3255

Received September 30, 2006; E-mail: adams@mail.chem.sc.edu; hall@science.tamu.edu

Abstract: The compound $Pt_3Re_2(CO)_6(PBu^t_3)_3$, **1**, was obtained from the reaction of $Re_2(CO)_{10}$ with $Pt(PBu^t_3)_2$ in octane solvent at reflux. Compound **1** consists of a trigonal bipyramidal cluster of five metal atoms with three platinum atoms in the trigonal plane and the two rhenium atoms in the apical positions. The metal cluster is formally unsaturated by 10 electrons. Compound **1** sequentially adds 3 equiv of hydrogen at room temperature/1 atm to form the series of compounds $Pt_3Re_2(CO)_6(PBu^t_3)_3(\mu\text{-}H)_2$, **2**, $Pt_3Re_2(CO)_6(PBu^t_3)_3(\mu\text{-}H)_4$, **3**, and $Pt_3Re_2(CO)_6(PBu^t_3)_3(\mu\text{-}H)_6$, **4**. A small but significant kinetic isotope effect was observed, $k_H/k_D = 1.3$. The rate of addition of hydrogen is unaffected by the presence of a 20-fold excess of free PBu^t_3 in solutions of **1**. Compounds **2**−**4** each consist of a trigonal bipyramidal cluster of three platinum and two rhenium atoms similar to that of **1**. The hydrido ligands in **2**−**4** bridge the platinum−rhenium bonds and are arranged to give structures having overall C_{2v} symmetry for **2** and **3** and approximate D_{3h} symmetry for **4**. Some of the hydrido ligands were expelled from **4** in the form of hydrogen upon exposure of solutions to UV−vis irradiation to yield compound **3** and then **2** in reasonable yields, but the elimination of all hydrido ligands to yield **1** was achieved only under the most forcing UV irradiation and then only with a major loss of the complex due to decomposition. The electronic structures of **1**−**4** were investigated by DFT calculations. Additional DFT calculations have suggested some mechanisms for the activation of hydrogen at multicenter metal sites without ligand eliminations prior to the hydrogen additions.

Introduction

There is currently much interest in the development of a hydrogen-based system for fuels and energy storage for the future.[1] There are active searches for molecules and materials that can reversibly absorb large quantities of hydrogen.[2,3] Studies have shown that in the presence of bulky phosphine ligands certain metal complexes will react with hydrogen to condense and form polynuclear metal cluster complexes containing unusually large numbers of hydrido ligands.[4,5] Recent studies have shown that even some cyclopentadienyl complexes of the lanthanides can form polynuclear metal complexes containing large numbers of hydrido ligands.[6] Reversibility is a property that must be central to any application of new materials for hydrogen storage. There are only a few examples of thermally reversible hydrogen additions to metal complexes that are not accompanied by the addition and elimination of other ligands.[4a,b,7,8] One of the most interesting families of these compounds are

† University of South Carolina.
‡ Texas A&M University.

(1) (a) DOE Hydrogen Storage Targets. http://www.eere.energy.gov/hydrogenandfuelcells/mypp/pdfs/storage.pdf. (b) *A Multiyear Plan for the Hydrogen R&D Program: Rationale, Structure, and Technology Road Maps*; U.S. Department of Energy: Washington, DC, 1999; http://www.eere.energy.gov/ hydrogenandfuelcells/pdfs/bk28424.pdf, p 32. (c) *National Hydrogen Energy Road Map*; U.S. Department of Energy: Washington, DC, 2002; http://www.sc.doe.gov/bes/reports/files/NHE_rpt.pdf, p 17. (d) Ogden, J. M. *Phys. Today* **2002**, *55*, 69−75. (e) Ogden, J. M. *Annu. Rev. Energy Environ.* **1999**, *24*, 227−279. (f) Ogden, J. *Sci. Am.* **2006**, *295*, 94−101.
(2) (a) Schlapbach. L; Züttel, A. *Nature* **2001**, *414*, 353−358. (b) Zecchina, A.; Borgida, S.; Vitillo, J. G.; Ricchiardi, G.; Lamberti, C.; Spoto, G.; Bjørgen, M.; Lillerud, K. P. *J. Am. Chem. Soc.* **2005**, *127*, 6361−6366. (c) Nijkamp, M. G.; Raaymakers, J. E. M. J.; van Dillen, A. J.; de Jong, K. P. *Appl. Phys. A* **2001**, *72*, 619−623. (d) Weitkamp, J.; Fritz, M.; Ernst, S. *Int. J. Hydrogen Energy* **1995**, *20*, 967−970.
(3) (a) Rosi, N. L.; Eckert, J.; Eddaoudi, M.; Vodak, D. T.; O'Keerre, M.; Yaghi, O. M. *Science* **2003**, *300*, 1127−1129. (b) Zhao, X.; Xiao, B.; Fletcher, A. J.; Thomas, K. M.; Bradshaw, D.; Rosseinsky, M. J. *Science* **2004**, *306*, 1012−1015. (c) Rowsell, J. L. C.; Eckert, J.; Yaghi, O. M. *J. Am. Chem. Soc.* **2005**, *127*, 14904−14099. (d) Rowsell, J. L. C.; Spencer, E. C.; Eckert, J.; Howard, J. A. K.; Yaghi, O. M. *Science* **2005**, *309*, 1350−1354. (e) Rowsell, J. L. C.; Yaghi, O. M. *Angew. Chem., Int. Ed.* **2005**, *44*, 4670−4679. (f) Dinca, M.; Long, J. R. *J. Am. Chem. Soc.* **2005**, *127*, 9376−9377. (g) Kaye, S. S.; Long, J. R. *J. Am. Chem. Soc.* **2005**, *127*, 6506−6507. (h) Sun, D.; Ma, S.; Ke, Y.; Collins, D. J.; Zhou, H.-C. *J. Am. Chem. Soc.* **2006**, *128*, 3896−3897.
(4) (a) Brayshaw, S. K.; Ingleson, M. J.; Green, J. C.; McIndoe, J. S.; Raithby, P. R.; Kociok-Köhn, G.; Weller, A. S. *J. Am. Chem. Soc.* **2006**, *128*, 6247−6263. (b) Brayshaw, S. K.; Ingleson, M. J.; Green, J. C.; Raithby, P. R.; Kociok-Köhn, G.; McIndoe, J. S.; Weller, A. S. *Angew. Chem., Int. Ed.* **2005**, *44*, 6875−6878. (c) Ingleson, M. J.; Mahon, M. F.; Raithby, P. R.; Weller, A. S. *J. Am. Chem. Soc.* **2004**, *126*, 4784−4785.
(5) (a) Frost, P. W.; Howard, J. A. K.; Spencer, J. L.; Turner, D. G. *J. Chem. Soc., Chem. Commun.* **1981**, 1104−1106. (b) Gregson, D.; Howard, J. A. K.; Murray, M.; Spencer, J. L. *J. Chem. Soc., Chem. Commun.* **1981**, 716−717. (c) Chodosh, D. F.; Crabtree, R. H.; Felkin, H.; Morehouse, S.; Morris, G. E. *Inorg. Chem.* **1982**, *21*, 1307−1311. (d) Smidt, S. P.; Pfaltz, A.; Martinez-Viviente, E.; Pregosin, P. S.; Albinati, A. *Organometallics* **2003**, *22*, 1000−1009. (e) Lemmen, T. H.; Folting, K.; Huffman, J. C.; Caulton, K. G. *J. Am. Chem. Soc.* **1985**, *107*, 7774−7775. (f) Goeden, G. V.; Caulton, K. G. *J. Am. Chem. Soc.* **1981**, *103*, 7354−7355.
(6) (a) Tardif, O.; Nishiura, M.; Hou, Z. M. *Organometallics* **2003**, *22*, 1171−1173. (b) Cui, D. M.; Tardif, O.; Hou, Z. M. *J. Am. Chem. Soc.* **2004**, *126*, 1312−1313. (c) Luo, Y.; Baldamus, J.; Tardif, O.; Hou, Z. M. *Organometallics* **2005**, *24*, 4362−4366.
(7) Kubas, G. J. *Metal Dihydrogen and σ-Bond Complexes*; Kluwer/Academic/Plenum Publishers: New York, 2001; Chapter 3.

 10.1021/ja067028g CCC: $37.00 **© 2007 American Chemical Society**

Scheme 1

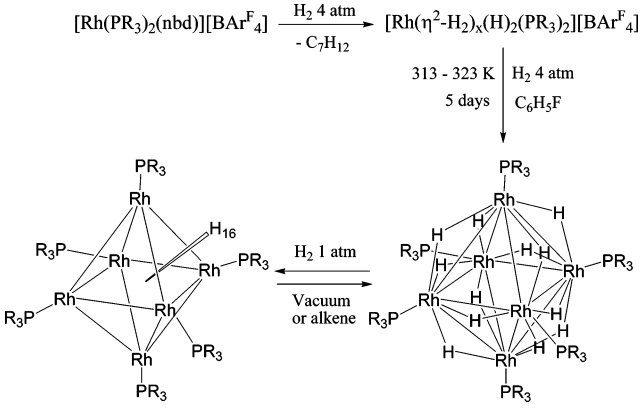

Scheme 2[a]

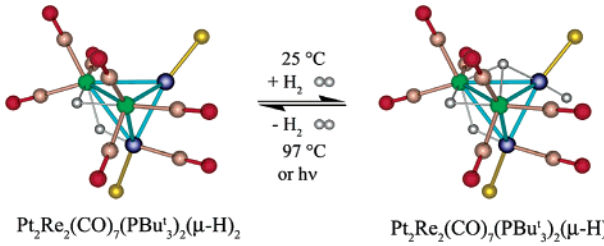

[a] Key: platinum (blue), rhenium (green), phosphorus (gold), oxygen (red), carbon (pink), hydrogen (gray).

the hexarhodium complexes $[Rh_6(PR_3)_6H_{12}][BAr^F_4]_2$ (R = ^{i}Pr, Cy; Ar^F = $[B\{C_6H_3(CF_3)_2\}_4]$) that were recently reported by Weller and co-workers.[4] These complexes add an additional 2 equiv of hydrogen, reversibly, to yield the hexadecahydride complexes $[Rh_6(PR_3)_6H_{16}][BAr^F_4]_2$ (R = ^{i}Pr, Cy; Ar^F = $[B\{C_6H_3(CF_3)_2\}_4]$); see Scheme 1.[4a,b] Another example is the unsaturated dirhenium diplatinum complex $Pt_2Re_2(CO)_7(PBu^t_3)_2$-($\mu$-H)$_2$, which adds 1 equiv of H_2 at room temperature to yield the tetrahydrido complex $Pt_2Re_2(CO)_7(PBu^t_3)_2(\mu$-H)$_4$.[8c] Interestingly, this hydrogen addition can be reversed by both thermal and photochemical means; see Scheme 2. Photochemical stimulation is an effective method for releasing hydrogen from mononuclear metal complexes,[9] but there are very few examples where hydrogen can be eliminated photolytically from a polynuclear metal complex.[8c]

Electronic unsaturation is an important condition for the addition of small molecules such as H_2 to polynuclear metal complexes.[4,7,8a–d] In most cases, hydrogen addition reactions follow a ligand elimination step that creates an electronically unsaturated intermediate.[8e] Bulky ligands, such as PBu^t_3, can stabilize metal complexes in electronically unsaturated states; see above. In these cases, it is possible that hydrogen addition can proceed without a ligand elimination step.[7,8c]

In recent studies we have shown that it is possible to prepare electronically unsaturated *bi*metallic cluster complexes by introducing the 12-electron Pt(PBu^t_3) or Pd(PBu^t_3) group into metal carbonyl clusters through use of the reagents Pd(PBu^t_3)$_2$ and Pt(PBu^t_3)$_2$.[10–13] In many cases, the M(PBu^t_3), M = Pd or Pt, groups in these complexes are highly mobile and readily move about the surface of the cluster complex itself.[11] To some of these compounds we have been able to introduce simple small molecules such as H_2[8c,9,14] and alkynes.[15] Here, we present a new example of these unsaturated complexes, the highly unsaturated compound $Pt_3Re_2(CO)_6(PBu^t_3)_3$, **1**, which sequentially adds up to 3 equiv of hydrogen at room temperature/1 atm of H_2 in a process that can be reversed partially by application of UV–vis irradiation. A preliminary report of a portion of this work has been published.[16]

Experimental Section

General Data. Reagent grade solvents were dried by the standard procedures and were freshly distilled prior to use. Infrared spectra were recorded on a Thermo Nicolet Avatar 360 FT-IR spectrophotometer. ^{1}H NMR and ^{31}P{^{1}H} NMR spectra were recorded on a Varian Mercury 400 spectrometer operating at 400.1 and 161.9 MHz, respectively. The ^{1}H NMR spectrum of **2** was recorded on a Varian Inova 500 spectrometer operating at 500.2 MHz. ^{31}P{^{1}H} NMR spectra were externally referenced against 85% ortho-H_3PO_4. NMR simulations were performed using the SpinWorks program.[17] Electrospray mass spectrometric measurements were obtained on a MicroMass Q-Tof spectrometer. Pt(PBu^t_3)$_2$ and $Re_2(CO)_{10}$ were purchased from Strem and were used without further purification. Product separations were performed by thin layer chromatography (TLC) in air on Analtech 0.25 and 0.5 mm silica gel 60 Å F_{254} glass plates.

Preparation of $Pt_3Re_2(CO)_6(PBu^t_3)_3$, 1. Under an atmosphere of nitrogen, $Re_2(CO)_{10}$ (29.0 mg, 0.044 mmol) and Pt(PBu^t_3)$_2$ (160.0 mg, 0.267 mmol) were dissolved in 15 mL of octane. The reaction mixture was heated to reflux for 3 h. The solvent was removed in vacuo, and the product was separated by TLC by using a 3:1 hexane/methylene chloride solvent mixture to yield 13.9 mg (18%) of brown **1**. A considerable amount of $Re_2(CO)_{10}$, 8.8 mg (30%), was recovered along with one minor dirhenium product, $Re_2(CO)_9(PBu^t_3)$, 4.0 mg (11%), a phosphine derivative of $Re_2(CO)_{10}$. Spectral data for **1**: IR ν_{CO} (cm^{-1}, in hexane) 1985 (s), 1892 (s); ^{1}H NMR (400 MHz, toluene-d_8, 25 °C, TMS) δ =1.63 ppm (d, ^3J(P,H) = 13 Hz, 81 H, CH_3); ^{31}P{^{1}H} NMR (162 MHz, toluene-d_8, 25 °C, 85% ortho-H_3PO_4) δ = 109.23 ppm (m, 3P) [^2J(Pt,P$_a$) = 332 Hz, ^3J(P$_a$,P$_b$) = 44 Hz] [^1J(Pt,P$_b$) = 4162 Hz, ^3J(P$_a$,P$_b$) = 44 Hz] [^1J(Pt,P$_b$) = 4531 Hz] [^2J(Pt,P$_a$) = 1253 Hz]; ES$^+$/MS *m*/*z* calcd for M + H, $[Pt_3Re_2P_3O_6C_{42}H_{81} + H]^+$, 1733, found 1733. The isotope pattern is consistent with the presence of three platinum and two rhenium atoms. Anal. Calcd for **1**: 29.07, C; 4.71, H. Found:

(8) (a) Farrugia, L. J.; Green, M.; Hankey, D. R.; Orpen, A. G.; Stone, F. G. A. *J. Chem. Soc., Chem. Commun.* **1983**, 310–312. (b) Adams, R. D.; Wang, S. *Organometallics* **1986**, *5*, 1272–1274. (c) Adams, R. D.; Captain, B.; Smith, M. D. *Angew. Chem., Int. Ed.* **2006**, *45*, 1109–1112. (d) Aubart, M. A.; Chandler, B. D.; Gould, R. A. T.; Krogstad, D. A.; Schoondergang, M. F. J.; Pignolet, L. H. *Inorg. Chem.* **1994**, *33*, 3724–3734. (e) Safarowic, F. J.; Bierdeman, D. J.; Keister, J. B. *J. Am. Chem. Soc.* **1996**, *118*, 11805–11812. (f) Arif, A. M.; Bright, T. A.; Jones, R. A.; Nunn, C. M. *J. Am. Chem. Soc.* **1988**, *110*, 6894–6895.

(9) (a) Perutz, R. N. *Pure Appl. Chem.* **1998**, *70*, 2211–2220. (b) Geoffroy, G. L.; Wrighton, M. S. *Organometallic Photochemistry*; Academic Press: New York, 1979; Chapter 7. (c) Daniel, C. *J. Phys. Chem.* **1991**, *95*, 2394–2398. (d) Geoffroy, G. L. *Prog. Inorg. Chem.* **1980**, *27*, 123–151. (d) Ma, Y.; Bergman, R. G. *Organometallics* **1994**, *13*, 2548–2550. (e) Janowicz, A. H.; Bergman, R. G. *J. Am. Chem. Soc.* **1983**, *105*, 3929–3939.

(10) (a) Adams, R. D.; Captain, B.; Fu, W.; Hall, M. B.; Manson, J.; Smith, M. D.; Webster, C. E. *J. Am. Chem. Soc.* **2004**, *126*, 5253–5267. (b) Adams, R. D.; Captain, B.; Fu, W.; Smith, M. D. *J. Am. Chem. Soc.* **2002**, *124*, 5628–5629. (c) Adams, R. D.; Captain, B.; Zhu, L. *Inorg. Chem.* **2006**, *45*, 430–436.

(11) (a) Adams, R. D.; Captain, B.; Fu, W.; Pellechia, P. J.; Smith, M. D. *Angew. Chem., Int. Ed.* **2002**, *41*, 1951–1953. (b) Adams, R. D.; Captain, B.; Fu, W.; Pellechia, P. J.; Smith, M. D. *Inorg. Chem.* **2003**, *42*, 2094–2101. (c) Adams, R. D.; Captain, B.; Fu, W.; Pellechia, P. J.; Zhu, L. *Inorg. Chem.* **2004**, *43*, 7243–7249.

(12) Adams, R. D.; Captain, B.; Hall, M. B.; Smith, J. L., Jr.; Webster, C. E. *J. Am. Chem. Soc.* **2005**, *127*, 1007–1014.

(13) Adams, R. D.; Captain, B.; Herber, R. H.; Johansson, M.; Nowik, I.; Smith, J. L., Jr.; Smith, M. D. *Inorg. Chem.* **2005**, *44*, 6346–6358.

(14) Adams, R. D.; Captain, B.; Zhu, L. *Inorg. Chem.* **2005**, *44*, 6623–6631.

(15) Adams, R. D.; Captain, B.; Zhu, L. *Organometallics* **2005**, *24*, 2419–2423.

(16) Adams, R. D.; Captain, B. *Angew. Chem., Int. Ed.* **2005**, *44*, 2531–2533.

(17) Marat, K. SpinWorks version 2.4. Department of Chemistry, University of Manitoba, Winnipeg, Manitoba, Canada R3T 2N2; ftp://davinci.chem.umanitoba.ca/pub/marat/SpinWorks/.

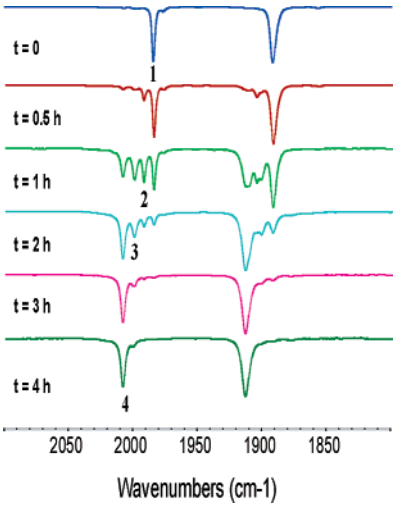

Figure 1. IR spectra in the CO absorption region showing the progress of the reaction of **1** with hydrogen to form **2**−**4** as a function of time. Reaction times *t* in hours are shown in the insets on the left.

29.98, C; 4.89, H. Spectral and crystallographic data for $Re_2(CO)_9(PBu^t_3)$: IR ν_{CO} (cm^{-1}, in hexane) 2109 (m), 2004 (vs), 1970 (m), 1920 (s); ^1H NMR (400 MHz, toluene-d_8, 25 °C, TMS) δ = 1.19 ppm (d, $^3J(P,H)$ = 12 Hz, 27 H, CH_3); $^{31}P\{^1H\}$ NMR (162 MHz, toluene-d_8, 25 °C, 85% ortho-H_3PO_4) δ = 88.47 ppm (s, 1P); monoclinic, space group $P2_1/n$, unit cell a = 11.7770(11) Å, b = 14.9566(15) Å, c = 45.768(5) Å, α = 90.00°, β = 92.098(2)°, γ = 90.00°, V = 8056.3(14) Å^3, and Z = 12, temperature 294(2) K, radiation Mo Kα (λ = 0.71073 Å), number of reflections ($>2\sigma$) 10887, number of parameters 917, R = 0.0331, R_w = 0.0745.

Addition of Hydrogen to 1. Compound **1** (11.6 mg, 0.0067 mmol) was dissolved in 25 mL of hexane. With stirring, hydrogen was then allowed to purge through the solution at 25 °C for 4 h. The solvent was removed in vacuo, and the product was separated by TLC using a 3:1 hexane/methylene chloride solvent mixture to yield 10.5 mg (90%) of orange $Pt_3Re_2(CO)_6(PBu^t_3)_3(\mu\text{-}H)_6$, **4**. Spectral data for **4**: IR ν_{CO} (cm^{-1}, in hexane) 2009 (s), 1914 (vs); ^1H NMR (400 MHz, toluene-d_8, 25 °C, TMS) δ = 1.50 ppm (d, $^3J(P,H)$ = 13 Hz, 81 H, CH_3), −4.34 ppm (quartet, $^1J(Pt,H)$ = 723 Hz, $^2J(P,H)$ = 4 Hz, 6H, hydride); $^{31}P\{^1H\}$ NMR (162 MHz, toluene-d_8, 25 °C, 85% ortho-H_3PO_4) 111.42 ppm (m, 3P) [$^2J(Pt,P_a)$ = 222 Hz, $^3J(P_a,P_b)$ = 56 Hz] [$^1J(Pt,P_b)$ = 2986 Hz, $^3J(P_a,P_b)$ = 56 Hz] [$^1J(Pt,P_b)$ = 3208 Hz, $^3J(P_a,P_b)$ = 56 Hz], see the Discussion for an explanation; ES^+/MS m/z calcd for M + H, $[Pt_3Re_2P_3O_6C_{42}H_{87} + H]^+$, 1739, found 1739. The isotope pattern is consistent with the presence of three platinum and two rhenium atoms. Anal. Cacld for $Pt_3Re_2(CO)_6(PBu^t_3)_3(\mu\text{-}H)_6{\cdot}C_6H_6$: 31.73, C; 5.16, H. Found: 31.94, C; 5.21, H. If one follows the reaction of **1** with hydrogen at 25 °C/1 atm by IR spectroscopy, CO absorptions due to the formation of a series of three products, $Pt_3Re_2(CO)_6(PBu^t_3)_3(\mu\text{-}H)_2$, **2**, $Pt_3Re_2(CO)_6(PBu^t_3)_3(\mu\text{-}H)_4$, **3**, and $Pt_3Re_2(CO)_6(PBu^t_3)_3(\mu\text{-}H)_6$, **4**, are observed, formed by the addition of 1, 2, and 3 equiv of H_2 to **1**. Plots of a series of these spectra as a function of time are shown in Figure 1. Absorptions due to compounds **2** and **3** are observed at 1992 (vs), 1905 (s), and 1893 (s) cm^{-1} and 2000 (vs), 1910 (s), and 1901 (s) cm^{-1}, respectively. Compound **2** is sensitive to air and silica gel. It was obtained in a pure form only by irradiating solutions of **4**; see below. Compound **3** can be isolated in a low yield by stopping the reaction before completion; see the next section.

Preparation of $Pt_3Re_2(CO)_6(PBu^t_3)_3(\mu\text{-}H)_4$, 3. Compound **1** (16.3 mg, 0.0094 mmol) was dissolved in 25 mL of hexane. With stirring, hydrogen was then allowed to purge through the solution at 25 °C for 1.5 h. The solvent was removed in vacuo, and the products were separated by TLC using a 4:1 hexane/methylene chloride solvent mixture to yield 2.1 mg (13%) of brown **3** and 2.4 mg (15%) of orange **4**. Spectral data for **3**: IR ν_{CO} (cm^{-1}, in hexane) 2000 (vs), 1910 (s), 1901 (s); ^1H NMR (400 MHz, toluene-d_8, 25 °C, TMS) δ = 1.63 ppm (d, $^3J(P,H)$ = 13 Hz, 27 H, CH_3), 1.47 ppm (d, $^3J(P,H)$ = 13 Hz, 54 H, CH_3), −7.42 ppm (m, $^1J(Pt,H)$ = 760 Hz, 4H, hydride); $^{31}P\{^1H\}$ NMR (162 MHz, toluene-d_8, 25 °C, 85% ortho-H_3PO_4) δ = 110.65 ppm (m, 2P), 108.41 ppm (m, 1p) [$^3J(P_A,P_B)$ = 55.0 Hz]; ES^+/MS m/z calcd for M + H, $[Pt_3Re_2P_3O_6C_{42}H_{85} + H]^+$, 1737, found 1737. The isotope pattern is consistent with the presence of three platinum and two rhenium atoms.

Determination of the Kinetic Isotope Effect (KIE) for the Addition of H_2 to 1. At room temperature, deuterium gas was bubbled (flow rate ~27 mL/min) through the solution of 6.0 mg of **1** dissolved in 25 mL of hexane. During this time IR spectra were recorded periodically. Under identical conditions, hydrogen was bubbled through a solution of **1** (6.0 mg) dissolved in 25 mL of hexane, and the IR spectra were recorded periodically. At certain times the IR spectra of the two samples appeared to be virtually the same. The KIE was determined to be the ratio of the reaction times for D_2/H_2 for the two reactions when the spectra appeared to be the same. For example, the IR spectrum for the D_2 addition reaction after 2 h was approximately the same as the IR spectrum after 1.5 h for the H_2 addition reaction; thus, the D_2/H_2 isotope effect k_H/k_D was determined to be 1.3(1).

Addition of H_2 to 1 in the Presence of Free PBu^t_3. Compound **1** (11.0 mg, 0.006 mmol) was dissolved in 40 mL of hexane. This solution was divided into two equal portions, and to one of these solutions was added PBu^t_3 (16 μL, 0.064 mmol). With stirring, hydrogen gas was then bubbled through both solutions at equal rates for 3 h. A series of IR spectra for the two samples were recorded during the 3 h period. Comparison of the IR spectra recorded at the same time intervals indicated no significant differences in the rate of formation of compounds **2**−**4** in the presence or absence of PBu^t_3.

UV−Vis Irradiation of 4. Compound **4** (10.1 mg, 0.0058 mmol) was dissolved in 40 mL of toluene in a 100 mL three-neck Pyrex flask equipped with a reflux condenser and a gas inlet. A slow stream of nitrogen (flow rate ~27 mL/min) was allowed to flow through the flask while the solution was irradiated for 7.5 h using a medium-pressure mercury UV lamp (1000 W). The progress of this reaction can be monitored by IR. The toluene solvent was then removed in vacuo, and the residue was dissolved in ~40 mL of hexane. The hexane solution was then filtered through a glass frit into a 100 mL Schlenk flask. The hexane solution was concentrated to ~5 mL and then transferred to a 10 mL Schlenk tube. This solution was further concentrated to 1−2 mL and then placed in the freezer (−25 °C) overnight to yield dark crystals of **2** (2.7 mg, 27%) (*note: compound 2 is unstable on silica gel and decomposes in air*): IR ν_{CO} (cm^{-1}, in hexane) 1992 (vs), 1905 (s), 1893 (s); ^1H NMR (400 MHz, toluene-d_8, 25 °C, TMS) δ = 1.56 ppm (d, $^3J(P,H)$ = 13 Hz, 27 H, CH_3), 1.52 ppm (d, $^3J(P,H)$ = 13 Hz, 54 H, CH_3), −5.91 ppm (dt, $^1J(Pt,H)$ = 821 Hz, $^2J(P,H)$ = 7.6 Hz, $^3J(P,H)$ = 1.4 Hz, 2H, hydride); $^{31}P\{^1H\}$ NMR (162 MHz, toluene-d_8, 25 °C, 85% ortho-H_3PO_4) δ = 111.1 ppm (d, $^3J(P,P)$ = 53 Hz, 2P), 105.6 ppm (t, $^3J(P,P)$ = 53 Hz, 1P); ES^+/MS m/z calcd for M + H, $[Pt_3Re_2P_3O_6C_{42}H_{83} + H]^+$, 1735, found 1735. The isotope pattern is consistent with the presence of three platinum and two rhenium atoms.

Photolysis of Compound 4 in Quartz Glassware. Compound **4** (10.5 mg, 0.0060 mmol) was dissolved in 30 mL of hexane in a 50 mL three-neck quartz flask equipped with a reflux condenser and a gas inlet. A slow stream of nitrogen (flow rate ~27 mL/min) was allowed to flow through the flask while the solution was irradiated for 4 h by using a high-pressure mercury UV lamp (American Ultraviolet Co.) at the 250 wpi setting. The IR spectrum of the reaction mixture showed compound **2** to be the major product; however, a small absorption for compound **1** was also observed. The solvent was removed in vacuo, and the product was separated by TLC using a 3:1 hexane/methylene chloride solvent mixture to yield a trace amount, ~0.5 mg (~ 0.5%), of compound **1**. The major compound **2** decomposed during

the separation, and bands corresponding to compounds **3** and **4** were also present in trace amounts.

Detection of H_2 by ^1H NMR. A 10.5 mg amount of **2** was dissolved in 3 mL of toluene-d_8 in a 10 mm NMR tube. The NMR tube was evacuated and filled with nitrogen four times and then evacuated one last time. The evacuated NMR tube was then irradiated using a medium-pressure mercury UV lamp (1000 W) for 5 h. ^1H NMR showed a singlet at 4.51 ppm, indicating the presence of H_2.

Crystallographic Analyses. Dark single crystals of **1** and **3** suitable for X-ray diffraction analyses were obtained by slow evaporation of solvent from a hexane/methylene chloride solvent mixture at −25 °C. Dark single crystals of **2** were obtained by slow evaporation of hexane at −25 °C. Red single crystals of **4** were obtained by slow evaporation from a benzene/octane solution at 8 °C. Each data crystal was glued onto the end of a thin glass fiber. X-ray intensity data were measured by using a Bruker SMART APEX CCD-based diffractometer using Mo Kα radiation ($\lambda = 0.71073$ Å). The raw data frames were integrated with the SAINT+ program by using a narrow-frame integration algorithm.[18] Correction for Lorentz and polarization effects was also applied with SAINT+. An empirical absorption correction based on the multiple measurement of equivalent reflections was applied using the program SADABS. All structures were solved by a combination of direct methods and difference Fourier syntheses and refined by a full-matrix least-squares method on F^2, using the SHELXTL software package.[19] All non-hydrogen atoms were refined with anisotropic displacement parameters. Hydrogen atoms were placed in geometrically idealized positions and included as standard riding atoms during the least-squares refinements. Crystal data, data collection parameters, and results of the analyses are listed in Tables 1 and 2.

Compounds **1**, **2**, and **4** crystallized in the monoclinic crystal system. For all three compounds, the systematic absences in the intensity data identified the unique space group $P2_1/n$. For compound **1** one molecule of hexane from the crystallization solvent cocrystallized with the complex. The solvent was included in the analysis and was satisfactorily refined with anisotropic thermal parameters. For compound **2** one molecule of hexane from the crystallization solvent cocrystallized with the complex. The solvent was included in the analysis and was satisfactorily refined with isotropic thermal parameters. For compound **4** one molecule of benzene and half a molecule of octane from the crystallization solvent cocrystallized with the complex. The solvent was included in the analysis and was satisfactorily refined with anisotropic thermal parameters. The six hydrido ligands in **4** were located and refined successfully with isotropic thermal parameters.

Compound **3** crystallized in the orthorhombic crystal system. The systematic absences in the intensity data were consistent with either space group *Pnma* or space group $Pna2_1$. The former space group was chosen initially for structure solution tests. This space group was confirmed by the successful solution and refinement of the structure. One molecule of hexane from the crystallization solvent was cocrystallized with the complex in the asymmetric unit. The solvent was included in the analysis and was satisfactorily refined with anisotropic thermal parameters.

Table 1. Crystallographic Data for Compounds **1** and **2**

	1	**2**
empirical formula	$Pt_3Re_2P_3O_6C_{42}H_{81}\cdot C_6H_{14}$	$Pt_3Re_2P_3O_6C_{42}H_{81}\cdot C_6H_{14}$
fw	1818.82	1818.82
cryst syst	monoclinic	monoclinic
lattice params		
a (Å)	13.9117(13)	13.9272(13)
b (Å)	24.058(2)	23.991(2)
c (Å)	18.0919(17)	18.0905(16)
β (deg)	92.210(2)	91.807(2)
V (Å^3)	6050.7(10)	6041.5(9)
space group	$P2_1/n$ (No. 14)	$P2_1/n$ (No. 14)
Z value	4	4
ρ_{calcd} (g/cm^3)	1.997	2.000
μ(Mo Kα) (mm^{-1})	11.016	11.033
temp (K)	296	296
$2\theta_{max}$ (deg)	50.06	50.06
no. of obsd reflns ($I > 2\sigma(I)$)	7040	5660
no. of params	559	529
GOF[a]	1.004	1.004
max shift in cycle	0.002	0.001
residuals:[a] R, R_w	0.0501, 0.1010	0.0515, 0.1068
abs correction	multiscan	multiscan
max/min	1.000/0.588	1.000/0.431
largest peak in final diff map (e$^-$/Å^3)	1.567	2.327

[a] $R = \sum_{hkl}(||F_o| - |F_c||)/\sum_{hkl}|F_o|$. $R_w = [\sum_{hkl}w(|F_o| - |F_c|)^2/\sum_{hkl}wF_o^2]^{1/2}$, $w = 1/\sigma^2(F_o)$. GOF $= [\sum_{hkl}w(|F_o| - |F_c|)^2/(n_{data} - n_{vari})]^{1/2}$.

Table 2. Crystallographic Data for Compounds **3** and **4**

	3	**4**
empirical formula	$Pt_3Re_2P_3O_6C_{42}H_{81}\cdot C_6H_{14}$	$Pt_3Re_2P_3O_6C_{42}H_{87}\cdot C_6H_6\cdot 1/2C_8H_{18}$
fw	1818.82	1873.92
cryst syst	orthorhombic	monoclinic
lattice params		
a (Å)	24.044(2)	14.7099(6)
b (Å)	18.2218(16)	23.4704(9)
c (Å)	13.8953(12)	17.7176(7)
β (deg)	90	91.031(1)
V (Å^3)	6087.9(9)	6116.0(4)
space group	*Pnma* (No. 61)	$P2_1/n$ (No. 14)
Z value	4	4
ρ_{calcd} (g/cm^3)	1.984	2.035
μ(Mo Kα) (mm^{-1})	10.949	10.902
temp (K)	296	100
$2\theta_{max}$ (deg)	56.72	56.60
no. of obsd reflns ($I > 2\sigma(I)$)	5638	13055
no. of params	308	641
GOF[a]	1.044	1.060
max shift in cycle	0.002	0.001
residuals:[a] R, R_w	0.0392, 0.0856	0.0342, 0.0757
abs correction	multiscan	multiscan
max/min	1.000/0.286	1.000/0.634
largest peak in final diff map (e$^-$/Å^3)	1.512	1.955

[a] $R = \sum_{hkl}(||F_o| - |F_c||)/\sum_{hkl}|F_o|$. $R_w = [\sum_{hkl}w(|F_o| - |F_c|)^2/\sum_{hkl}wF_o^2]^{1/2}$, $w = 1/\sigma^2(F_o)$. GOF $= [\sum_{hkl}w(|F_o| - |F_c|)^2/(n_{data} - n_{vari})]^{1/2}$.

Details of the Computational Treatments. All calculations were performed using the Gaussian 03 suite of programs.[20] Optimized gas-phase geometries for the QM model (see below) were obtained using the B3PW91 DFT method.[21,22] The basis set (BS1) used for geometry

(18) SAINT+ Version 6.2a. Bruker Analytical X-ray System, Inc., Madison, WI, 2001.
(19) Sheldrick; G. M. SHELXTL Version 6.1. Bruker Analytical X-ray Systems, Inc., Madison, WI, 1997.
(20) All calculations were conducted using the Gaussian03 suite of programs: Frisch, M. J.; Trucks, G. W.; Schlegel, H. B.; Scuseria, G. E.; Robb, M. A.; Cheeseman, J. R.; Montgomery, J. A., Jr.; Vreven, T.; Kudin, K. N.; Burant, J. C.; Millam, J. M.; Iyengar, S. S.; Tomasi, J.; Barone, V.; Mennucci, B.; Cossi, M.; Scalmani, G.; Rega, N.; Petersson, G. A.; Nakatsuji, H.; Hada, M.; Ehara, M.; Toyota, K.; Fukuda, R.; Hasegawa, J.; Ishida, M.; Nakajima, T.; Honda, Y.; Kitao, O.; Nakai, H.; Klene, M.; Li, X.; Knox, J. E.; Hratchian, H. P.; Cross, J. B.; Adamo, C.; Jaramillo, J.; Gomperts, R.; Stratmann, R. E.; Yazyev, O.; Austin, A. J.; Cammi, R.; Pomelli, C.; Ochterski, J. W.; Ayala, P. Y.; Morokuma, K.; Voth, G. A.; Salvador, P.; Dannenberg, J. J.; Zakrzewski, V. G.; Dapprich, S.; Daniels, A. D.; Strain, M. C.; Farkas, O.; Malick, D. K.; Rabuck, A. D.; Raghavachari, K.; Foresman, J. B.; Ortiz, J. V.; Cui, Q.; Baboul, A. G.; Clifford, S.; Cioslowski, J.; Stefanov, B. B.; Liu, G.; Liashenko, A.; Piskorz, P.; Komaromi, I.; Martin, R. L.; Fox, D. J.; Keith, T.; Al-Laham, M. A.; Peng, C. Y.; Nanayakkara, A.; Challacombe, M.; Gill, P. M. W.; Johnson, B.; Chen, W.; Wong, M. W.; Gonzalez, C.; Pople, J. A. Gaussian 03, Revision B.4. Gaussian, Inc., Pittsburgh, PA, 2003.
(21) Becke, A. D. *J. Chem. Phys.* **1993**, *98*, 5648−5652.

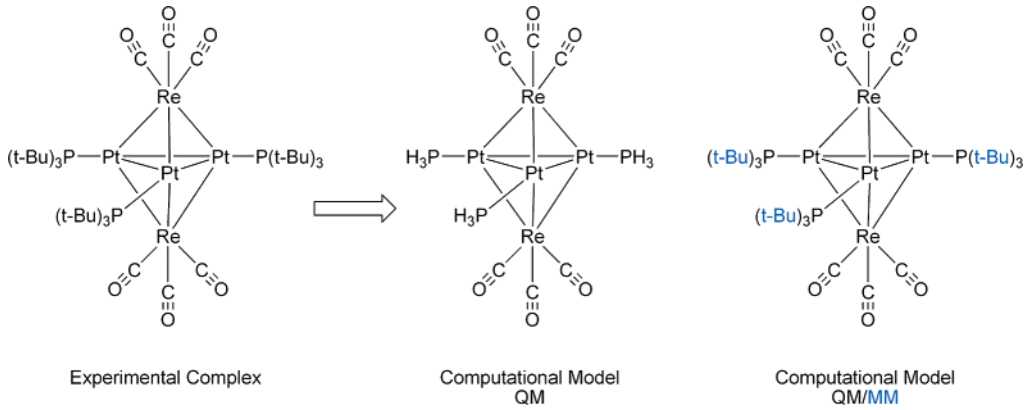

Figure 2. QM and QM/MM models used in the theoretical investigations. Text in blue indicates the regions that are modeled with molecular mechanics.

optimizations and energy calculations was implemented as follows: for rhenium and platinum, the valence double-ζ LANL2DZ[23] basis set was supplemented with sets of 6p functions for transition metals developed by Couty and Hall,[24] for phosphorus, the LANL2DZdp basis set was used,[24−26] for carbon and oxygen, the 6-31G(d′)[27] basis set was used, for the hydrogen atoms attached to phosphorus, the 6-31G basis set was used,[27] and for dihydrogen and for the hydrogen atoms that bonded to the platinum and rhenium, the 6-31G(d′,p′) basis set was used.[27] All structures were calculated in singlet spin states using the restricted B3PW91 method. Calculating the harmonic vibrational frequencies and noting the number of imaginary frequencies confirmed the nature of all intermediates ($N_{imag} = 0$) and transition-state structures ($N_{imag} = 1$).

Two computational models were used for the theoretical calculations: The first model, which will be referred to as the QM model, used a chemical model in which PH_3 ligands were used instead of the PBu^t_3 ligands and the geometry optimizations and energy calculations were conducted at the B3PW91/BS1 level of theory. The second model, which will be referred to as the QM/MM model, used the experimental chemical model; however, geometry optimizations and energy calculations were conducted using a two-level ONIOM procedure,[28] in which B3PW91/BS1 was used as the higher level of theory and the UFF molecular mechanics force field[29] was used as the lower level of theory. For the ONIOM procedure, $Re_2Pt_3(CO)_6(PH_3)_3$ was used as the structure of the high level (QM region), while $Re_2Pt_3(CO)_6(PBu^t_3)_3$ was used as the structure of the low level (MM region), as shown in Figure 2. Thus, the ONIOM-extrapolated electronic energy of the complex is given as follows:

$$\text{ONIOM-extrapolated energy of } [Re_2Pt_3(CO)_6(PBu^t_3)_3] = \text{B3PW91/BS1}[Re_2Pt_3(CO)_6(PH_3)_3] + \text{UFF}[Re_2Pt_3(CO)_6(PBu^t_3)_3] - \text{UFF}[Re_2Pt_3(CO)_6(PH_3)_3]$$

For QM/MM calculations that included dihydrogen or hydride ligands, the additional hydrogen atoms were also included in the QM region. An example of a Gaussian 03 input file for a QM/MM geometry optimization of $Re_2Pt_3(CO)_6(PBu^t_3)_3(\mu\text{-H})_6$ is provided in the Supporting Information. It should be noted that the choice of $Re_2Pt_3(CO)_6(PH_3)_3$ as the region for the high level of theory for the QM/MM model and as the chemical model for the QM model facilitates a comparison of the results obtained by the two approaches in terms of how the steric profile of the Bu^t groups influences the potential energy surface.

Results and Discussion

The new compound $Pt_3Re_2(CO)_6(PBu^t_3)_3$, **1**, was obtained in 18% yield as the only heterometallic product from the reaction of $Re_2(CO)_{10}$ with $Pt(PBu^t_3)_2$ in octane solvent at reflux (125 °C) for 3 h. Significant amounts of $Re_2(CO)_{10}$ were recovered from the reaction after this period, but longer reaction periods do not increase the yield of **1**. The only other product formed in this reaction was a monophosphine derivative of $Re_2(CO)_{10}$, $Re_2(CO)_9(PBu^t_3)$, obtained in 11% yield.[30] The $Re_2(CO)_9(PBu^t_3)$ product was characterized crystallographically. Its structure is similar to that of $Re_2(CO)_{10}$ with the exception of a PBu^t_3 ligand that occupies a coordination site *trans* to the Re−Re bond on one of the two rhenium atoms; see the Supporting Information for further details, Figure S1.

(22) (a) Burke, K.; Perdew, J. P.; Wang, Y. In *Electronic Density Functional Theory: Recent Progress and New Directions*; Dobson, J. F., Vignale, G., Das, M. P., Eds.; Plenum: New York, 1998; pp 81−111. (b) Perdew, J. P. In *Electronic Structure of Solids '91*; Ziesche, P., Eschrig, H., Eds.; Akademie Verlag: Berlin, 1991; p 11. (c) Perdew, J. P.; Chevary, J. A.; Vosko, S. H.; Jackson, K. A.; Pederson, M. R.; Singh, D. J.; Fiolhais, C. *Phys. Rev. B* **1992**, *46*, 6671−6687. (d) Perdew, J. P.; Chevary, J. A.; Vosko, S. H.; Jackson, K. A.; Pederson, M. R.; Singh, D. J.; Fiolhais, C. *Phys. Rev. B* **1993**, *48*, 4978. (e) Perdew, J. P.; Burke, K.; Wang, Y. *Phys. Rev. B* **1996**, *54*, 16533−16539.
(23) (a) Hay, P. J.; Wadt, W. R. *J. Chem. Phys.* **1985**, *82*, 270−283. (b) Wadt, W. R.; Hay, P. J. *J. Chem. Phys.* **1985**, *82*, 284−298. (c) Hay, P. J.; Wadt, W. R. *J. Chem. Phys.* **1985**, *82*, 299−310.
(24) Couty, M.; Hall, M. B. *J. Comput. Chem.* **1996**, *17*, 1359−1370.
(25) Basis sets were obtained from the Extensible Computational Chemistry Environment Basis Set Database, Version 02/25/04, as developed and distributed by the Molecular Science Computing Facility, Environmental and Molecular Sciences Laboratory, which is part of the Pacific Northwest Laboratory, P.O. Box 999, Richland, WA 99352, and funded by the U.S. Department of Energy. The Pacific Northwest Laboratory is a multiprogram laboratory operated by Battelle Memorial Institute for the U.S. Department of Energy under Contract DE-AC06-76.RLO 1830. Contact Karen Schuchardt for further information.
(26) Check, C. E.; Faust, T. O.; Bailey, J. M.; Wright, B. J.; Gilbert, T. M.; Sunderlin, L. S. *J. Phys. Chem. A* **2001**, *105*, 8111−8116.
(27) (a) Ditchfield, R.; Hehre, W. J.; Pople, J. A. *J. Chem. Phys.* **1971**, *54*, 724−728. (b) Hehre, W. J.; Ditchfield, R.; Pople, J. A. *J. Chem. Phys.* **1972**, *56*, 2257−2261. (c) Hariharan, P. C.; Pople, J. A. *Theor. Chim. Acta* **1973**, *28*, 213−222. (d) Petersson, G. A.; Al-Laham, M. A. *J. Chem. Phys.* **1991**, *94*, 6081−6090. (e) Petersson, G. A.; Bennett, A.; Tensfeldt, T. G.; Al-Laham, M. A.; Shirley, W. A.; Mantzaris, J. *J. Chem. Phys.* **1988**, *89*, 2193−2218. (f) Foresman, J. B.; Frisch, Æ. *Exploring Chemistry with Electronic Structure Methods*, 2nd ed.; Gaussian, Inc.: Pittsburgh, PA; 1996; p 110. The 6-31G(d′,p′) basis set has the d polarization functions for C, N, O, and F taken from the 6-311G(d) basis set, instead of those which use the exponent with the original arbitrarily assigned value of 0.8 used in the 6-31G(d) basis set.
(28) (a) Maseras, F.; Morokuma, K. *J. Comput. Chem.* **1995**, *16*, 1170−1179. (b) Humbel, S.; Sieber, S.; Morokuma, K. *J. Chem. Phys.* **1996**, *105*, 1959−1967. (c) Matsubara, T.; Sieber, S.; Morokuma, K. *Int. J. Quantum Chem.* **1996**, *60*, 1101−1109. (d) Svensson, M.; Humbel, S.; Froese, R. D. J.; Matsubara, T.; Sieber, S.; Morokuma, K. *J. Phys. Chem.* **1996**, *100*, 19357−19363. (e) Svensson, M.; Humbel, S.; Morokuma, K. *J. Chem. Phys.* **1996**, *105*, 3654−3661. (f) Dapprich, S.; Komáromi, I.; Byun, K. S.; Morokuma, K.; Frisch, M. J. *J. Mol. Struct.: THEOCHEM.* **1999**, *461−462*, 1−21. (g) Vreven, T.; Morokuma, K. *J. Comput. Chem.* **2000**, *21*, 1419−1432. (h) Vreven, T.; Morokuma, K.; Farkas, Ö.; Schlegel, H. B.; Frisch, M. J. *J. Comput. Chem.* **2003**, *24*, 760−769.
(29) Rappé, A. K.; Casewit, C. J.; Colwell, K. S.; Goddard, W. A.; Skiff, W. M. *J. Am. Chem. Soc.* **1992**, *114*, 10024−10035.
(30) See the Supporting Information for additional data on $Re_2(CO)_9(PBu^t_3)$.

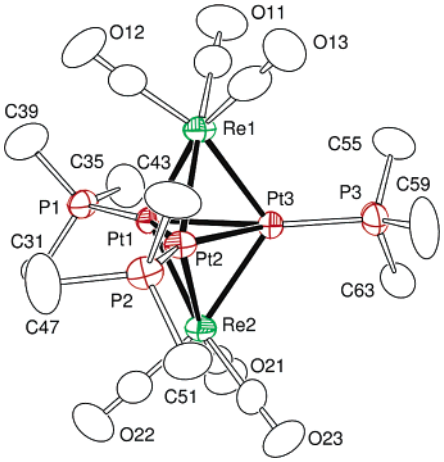

Figure 3. ORTEP diagram of the molecular structure of **1** showing 30% thermal ellipsoid probability. The methyl groups on the PBu^t_3 ligands are omitted for clarity.

Table 3. Comparison of the Metal–Metal Bond Distances (Å) for Compounds **1**–**4**

	1	2	3	4
Re(1)–Pt(1)	2.6275(7)	2.6915(8)	2.8132(4)	2.9202(3)
Re(1)–Pt(2)	2.6728(7)	2.7477(9)	2.8183(4)	2.8989(3)
Re(1)–Pt(3)	2.6431(7)	2.7343(8)	2.7887(4)	2.9004(3)
Re(2)–Pt(1)	2.6690(7)	2.7507(9)	2.8132(4)[a]	2.9170(3)
Re(2)–Pt(2)	2.6158(7)	2.6975(9)	2.8183(4)[a]	2.9134(3)
Re(2)–Pt(3)	2.6617(7)	2.7162(9)	2.7887(4)[a]	2.9050(3)
av Re–Pt	2.6483(7)	2.7230(9)	2.8067(4)	2.9092(3)
Pt(1)–Pt(2)	2.7202(7)	2.6771(8)	2.7165(5)	2.7026(3)
Pt(1)–Pt(3)	2.7104(7)	2.7521(8)	2.7366(5)	2.7095(3)
Pt(2)–Pt(3)	2.7369(7)	2.7497(8)	2.7406(5)	2.7259(3)
av Pt–Pt	2.7225(7)	2.7263(8)	2.7312(5)	2.7127(3)

[a] The bond distances are generated by symmetry equivalence in the molecule.

Compound **1** was isolated in a pure form by TLC with some loss due to decomposition. The compound was characterized by a single-crystal X-ray diffraction analysis, and an ORTEP diagram of its molecular structure is shown in Figure 3. Compound **1** contains a trigonal bipyramidal cluster of five metal atoms, three platinum and two rhenium. The three platinum atoms occupy the trigonal plane. The two rhenium atoms occupy the apical positions. Each platinum atom contains one PBu^t_3 ligand, and each rhenium atom contains three linear terminal carbonyl ligands. Ignoring the *tert*-butyl groups, the molecule has approximate D_{3h} symmetry. According to its formula, compound **1** contains only 62 valence electrons and is electronically unsaturated by 10 valence electrons according to conventional electron counting theories.[31,32] Selected bond distances for **1** are given in Table 3. The six Re–Pt bonds are unusually short. These bond distances range from 2.6158(7) to 2.6728(7) Å, av = 2.6483(7) Å. The Re–Pt bond distance in the linear compound $PtRe_2(CO)_{12}$ is 2.8309(5) Å.[33] The Pt–Re bond distances are similar to those in the electronically unsaturated tetrahedral Pt_3Re complex $[Pt_3Re(CO)_3(\mu\text{-dppm})_3]^+$, **5**, which are 2.6839(7), 2.6488(8), and 2.6850(8) Å.[34] The Pt–Pt distances in **1**, Pt(1)–Pt(2) = 2.7202(7) Å, Pt(1)–Pt(3) = 2.7104(7) Å, Pt(2)–Pt(3) = 2.7369(7) Å, av = 2.7225(7) Å, are longer than those in **5**, 2.6114(7), 2.6078(9), and 2.5930(9) Å. The IR spectrum of **1** shows only two CO stretching absorptions: 1985 (s) and 1892 (s) cm^{-1}. On the basis of D_{3h} symmetry, the higher energy absorption can be assigned to an A_2'' mode and the lower energy absorption to an E′ mode. The ^1H NMR spectrum exhibits only one resonance for the methyl groups, δ = 1.63 ppm (d, $^3J(P,H)$ = 13 Hz, 81 H, CH_3). The $^{31}P\{^1H\}$ NMR spectrum also shows only one resonance, δ =109.23 ppm, with satellites due to ^{195}Pt couplings; see Figure 4. The various ^{195}Pt isotopomers of **1**, **a**–**d**, are shown in Figure 5. Isomer **a** with no ^{195}Pt NMR active isotopes present (spin 0) gives rise to a single resonance (A in Figure 4) at 109.23 ppm. Isomer **b** with only one ^{195}Pt NMR nucleus (spin 1/2) gives rise to two doublets centered at 108.2 and 110.3 ppm [$^2J(Pt,P_a)$ = 332 Hz, $^3J(P_a,P_b)$ = 44 Hz] (B in Figure 4) and two triplets at 96.4 and 122.1 ppm [$^1J(Pt,P_b)$ = 4162 Hz, $^3J(P_a,P_b)$ = 44 Hz] (C in Figure 4). Isomer **c** gives rise to the resonances at 95.2 and 123.2 ppm [$^1J(Pt,P_b)$ = 4531 Hz] (D in Figure 4) and at 105.4 and 113.1 ppm [$^2J(Pt,P_a)$ = 1253 Hz] (E in Figure 4). The satellites for isomer **d** are not seen due to its very low relative abundance. The ^{195}Pt satellite pattern for **1** is similar to that observed for the compound $[Pt(PBu^t_3)(CO)]_3$.[35] Because of its high degree of electronic unsaturation, the reaction of **1** with hydrogen was investigated.

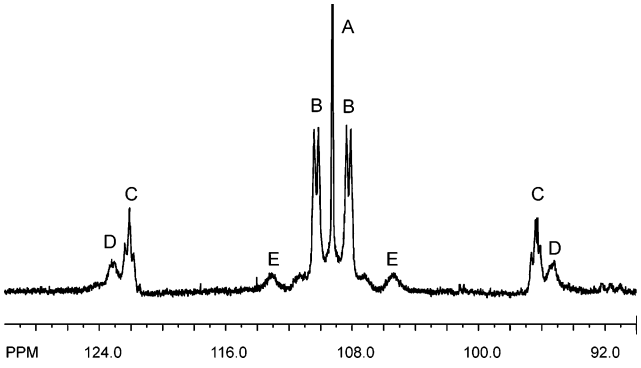

Figure 4. An enlarged version of the $^{31}P\{^1H\}$ NMR spectrum for compound **1**, showing the ^{195}Pt satellites. The center resonance A is truncated at this level of expansion.

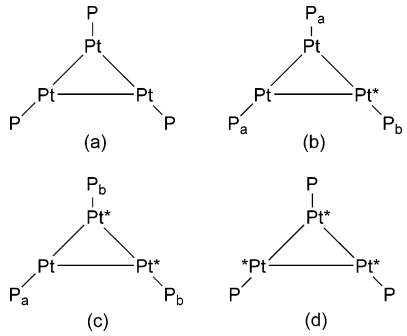

Figure 5. Illustration of the four magnetic isomers present in compound **1**. Pt and Pt* represent NMR-inactive Pt isotopes, spin 0, and the NMR-active isotope ^{195}Pt, spin 1/2, respectively.

Compound **1** reacts with hydrogen at 25 °C/ 1 atm to yield a series of three products: $Pt_3Re_2(CO)_6(PBu^t_3)_3(\mu\text{-}H)_2$, **2**, Pt_3-

(31) A trigonal bipyramidal cluster of five metal atoms in which each of the metal atoms formally has an 18-electron configuration will have a total of 72 valence electrons.[32]
(32) Mingos, D. M. P. *Introduction to Cluster Chemistry*; Prentice Hall: Engelwood Cliffs, NJ, 1990; Chapter. 2.
(33) Urbancic, M. A.; Wilson, S. R.; Shapley, J. R. *Inorg. Chem.* **1984**, *23*, 2954–2958.
(34) (a) Xiao, J.; Kristof, E.; Vittal, J. J.; Puddephatt, R. J. *J. Organomet. Chem.* **1995**, *490*, 1–6. (b) Xiao, J.; Puddephatt, R. J.; Manojlovic-Muir, L.; Muir, K. W.; Torabi, A. A. *J. Am. Chem. Soc.* **1994**, *116*, 1129–1130.
(35) Goel, R. G.; Ogini, W. O.; Srivastava, R. C. *J. Organomet. Chem.* **1981**, *214*, 405–417.

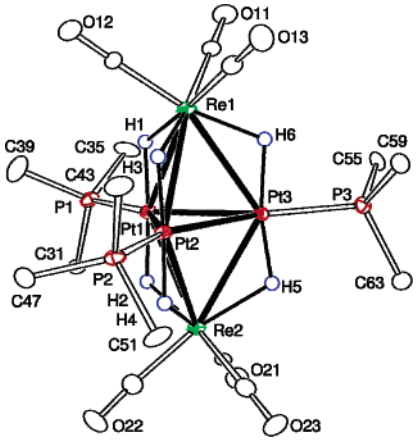

Figure 6. ORTEP diagram of the molecular structure of $Pt_3Re_2(CO)_6(PBu^t_3)_3(\mu\text{-}H)_6$, **4**, showing 50% thermal ellipsoid probability. The methyl groups on the PBu^t_3 ligands have been omitted for clarity.

$Re_2(CO)_6(PBu^t_3)_3(\mu\text{-}H)_4$, **3**, and $Pt_3Re_2(CO)_6(PBu^t_3)_3(\mu\text{-}H)_6$, **4**, formed by the addition of 1, 2, and 3 equiv of H_2 to **1**. A series of IR spectra which show the progress of the reaction as a function of time as monitored in the CO stretching region are presented in a stacked form in Figure 1.

After a period of 4 h, the air-stable compound **4** was isolated by TLC in 90% yield. Compound **4** was characterized by a combination of IR, ^{1}H NMR, ^{31}P NMR, mass spectra and a single-crystal X-ray diffraction analysis. An ORTEP diagram of the molecular structure of **4** is shown in Figure 6. Compound **4** is structurally similar to **1** except that it contains six additional hydrido ligands. All six hydrido ligands were located and refined in the structural analysis. There is one hydrido ligand bridging each of the six Pt−Re bonds of the Pt_3Re_2 trigonal bipyramidal cluster. As expected, the bridging hydrido ligands produce an increase in the length of the Pt−Re bonds relative to those in **1**, Pt(1)−Re(1) = 2.9202(3) Å, Pt(2)−Re(1) = 2.8989(3) Å, Pt(3)−Re(1) = 2.9004(3) Å, Pt(1)−Re(2) = 2.9170(3) Å, Pt(2)−Re(2) = 2.9134(3) Å, Pt(3)−Re(2) = 2.9050(3) Å, av = 2.9092(3) Å, an average increase of 0.26 Å.[36] The Pt−Pt distances in **4** are similar to those in **1**: Pt(1)−Pt(2) = 2.7026(3) Å, Pt(1)−Pt(3) = 2.7095(3) Å, Pt(2)−Pt(3) = 2.7259(3) Å, av = 2.7127(3) Å. Because of their close structural similarity, the IR spectrum of **4** in the CO region is very similar to that of **1**, except that the two absorptions have been shifted to higher energy: 2009 (s) and 1914 (vs) cm^{-1}. The ^{1}H NMR spectrum of **4** is similar to that of **1**, δ = 1.50 (d, ^3J(P,H) = 13 Hz, 81 H, CH_3), except for the presence of a new high-field multiplet at δ = −4.34 with coupling to the phosphorus and platinum atoms (^1J(Pt,H) = 723 Hz, ^2J(P,H) = 4 Hz, 6H) that is attributed to the six equivalent hydrido ligands. The multiplicity is a result of complex second-order coupling effects that are due to the magnetic nonequivalence of the hydrido ligands. The ^{31}P{^{1}H} NMR spectrum of **4** is very similar to that of **1**. Isomer **a** (see Figure 5) gives rise to a single resonance at 111.42 ppm (A in Figure 7). Isomer **b** gives rise to two doublets centered at 110.7 and 112.1 ppm [^2J(Pt,P_a) = 222 Hz, ^3J(P_a,P_b) = 56 Hz] (B in Figure 7) and two triplets at 102.2 and 120.6 ppm [^1J(Pt,P_b) = 2986 Hz, ^3J(P_a,P_b) = 56 Hz] (C in Figure 7), and isomer **c** gives rise to two doublets at 101.5 and 121.3 ppm [^1J(Pt,P_b) = 3208 Hz, ^3J(P_a,P_b) = 56 Hz] (D in Figure 7). The expected lines for P_a as well as those for isomer **d** are not seen due to their very low relative intensity.

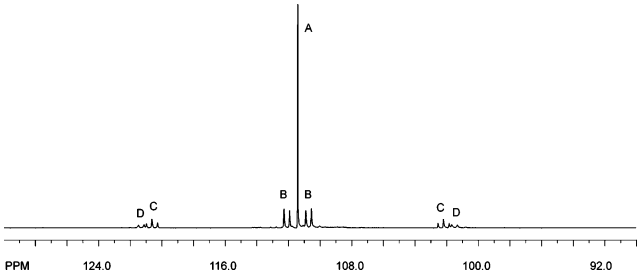

Figure 7. ^{31}P{^{1}H} NMR spectrum for compound **4**.

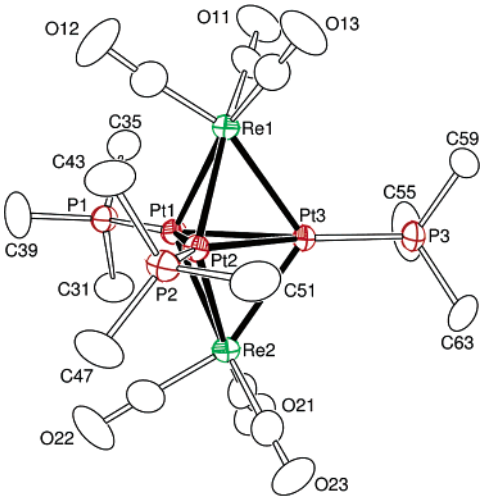

Figure 8. ORTEP diagram of the molecular structure of **2** showing 30% thermal ellipsoid probability. The methyl groups on the PBu^t_3 ligands have been omitted for clarity. The hydrido ligands were not located in the structural analysis.

Compound **3** can be isolated in a low yield by stopping the reaction before the conversion to **4** is complete and then separating by TLC. However, compound **2** is unstable to TLC and cannot be obtained in a significant amount by this method. A better route to **2** is via the photoelimination of hydrogen from **4**, see below, which provides **2** as the principal product. Compounds **2** and **3** were both characterized by a combination of IR, ^{1}H and ^{31}P NMR, mass spectra and single-crystal X-ray diffraction analyses. The arrangements of the non-hydrogen atoms in **2** and **3** are virtually the same as those of **1** and **4**; see Figures 8 and 9, except that the Pt−Re bonds become progressively and significantly longer as the number of hydrido ligands is increased. The hydrido ligands were not located in the structural analyses of **2** and **3**, presumably due to disorder, but they are believed to bridge the Pt−Re bonds because these bonds undergo progressive lengthening relative to those of **1**.[36] In particular, the average Pt−Re bond length in **2** is 2.7230(9) Å, and the average Pt−Re bond length in **3** is 2.8067(4) Å; see Table 3. The Pt−Pt bond distances in **2**, 2.7263(8) Å, and **3**, 2.7312(5) Å, are only slightly longer than those in **1** and **4**.

On the basis of their IR and NMR spectra and the energies of structures calculated using DFT calculations, it is proposed that compounds **2** and **3** both have structures with C_{2v} symmetry as shown in Figure 10. Due to their lower symmetry, the IR spectra of **2** and **3** both show three CO stretching absorptions at 1992 (vs), 1905 (s), and 1893 (s) cm^{-1} for **2** and 2000 (vs), 1910 (s), and 1901 (s) cm^{-1} for **3**. The presence of two lower

(36) Teller, R. G.; Bau, R. *Struct. Bonding* **1981**, *44*, 1−82.

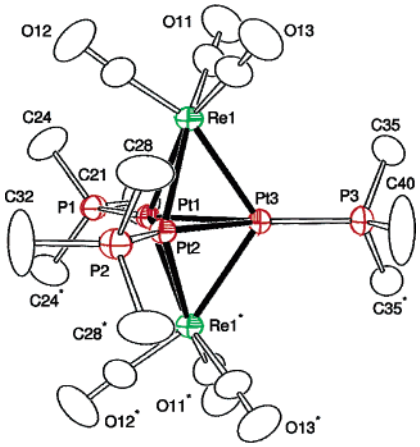

Figure 9. ORTEP diagram of the molecular structure of **3** showing 30% thermal ellipsoid probability. The methyl groups on the PBu^t_3 ligands have been omitted for clarity. The hydrido ligands were not located in the structural analysis.

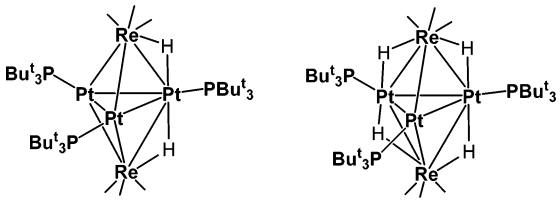

Figure 10. Structures for compounds **2** and **3** showing the proposed locations for the hydrido ligands based on spectral analyses and DFT calculations.

energy absorptions in both compounds can be attributed to a splitting of the degenerate lower energy E-mode that exists in the higher symmetry structure of **1**. The CO absorptions for **1**−**4** shift progressively to higher energy as the number of hydrido ligands is increased.

The ^{1}H NMR spectrum of **2** shows two doublets in a 1:2 ratio for the two inequivalent PBu^t_3 groups, $\delta = 1.56$ ppm (d, ^3J(P,H) = 13 Hz, 27 H, CH_3), 1.52 ppm (d, ^3J(P,H) = 13 Hz, 54 H, CH_3), and appropriately the ^{31}P{^{1}H} NMR spectrum shows a doublet and a triplet in a 2:1 ratio representing the A_2X first-order spin system, $\delta = 111.1$ ppm (d, ^3J(P,P) = 53 Hz), 105.6 ppm (t, ^3J(P,P) = 53 Hz). The resonance of the hydrido ligands in **2** shows coupling to both Pt and P at $\delta = -5.91$ (dt, ^1J(Pt,H) = 821 Hz, ^2J(P,H) = 7.6 Hz, ^3J(P,H) = 1.4 Hz, 2H); see Figure 11a. Spin simulation for the hydride resonance was carried out by using the values reported above. The simulated spectrum shown in Figure 11b represents the A_2MX_2 spin system. For a comparison the pattern representing an AA′MXX′ spin system is shown in Figure 11c. For the two hydrido ligands bonded to the same platinum atom, the simulated spectrum should be consistent with the A_2MX_2 pattern in Figure 11b. However, if the two hydride ligands were bonded to different platinum atoms, the expected spin system would be the AA′MXX′ pattern shown in Figure 11c. It is clear that the observed spectrum is most consisitent with a structure having the two hydrido ligands bonded to the same platinum atom.

As in compound **2**, the ^{1}H NMR spectrum of **3** shows two doublets in a 1:2 ratio for the methyl groups of the two

(37) Pavia, D. L.; Lampman, G. M.; Kriz, G. S. *Introduction to Spectroscopy*, 2nd ed.; Harcourt Brace: Orlando, FL, 1996; Chapter 5.

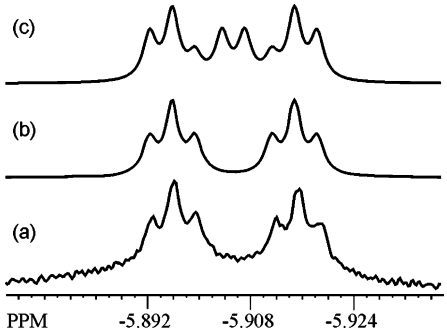

Figure 11. (a) ^{1}H NMR spectrum for compound **2**. (b) Simulated ^{1}H NMR spectrum for the second-order spin system A_2MX_2 for compound **2**. (c) Simulated ^{1}H NMR spectrum for the second-order spin system AA′MXX′ for compound **2**.

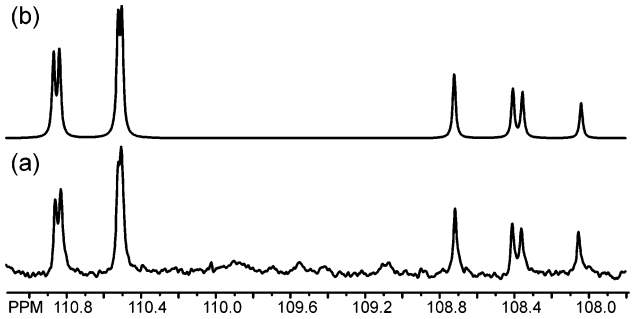

Figure 12. (a) Observed ^{31}P{^{1}H} NMR spectrum for compound **3**. (b) Simulated ^{31}P{^{1}H} NMR spectrum for the AB_2 second-order spin system for compound **3**.

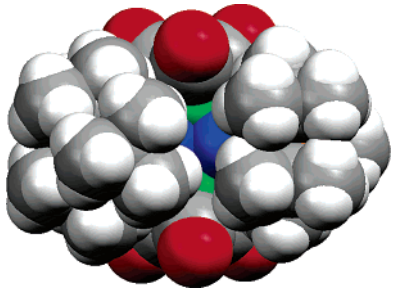

Figure 13. Space-filling model of the structure of **1** showing an opening between the *tert*-butyl groups of the $P(Bu^t)_3$ ligands above the Pt−Pt bond. Pt atoms are shown in blue, Re in green, O in red, C in gray, and H in white.

inequivalent PBu^t_3 ligands, $\delta = 1.56$ ppm (d, ^3J(P,H) = 13 Hz, 27 H, CH_3), 1.52 ppm (d, ^3J(P,H) = 13 Hz, 54 H, CH_3); however, the ^{31}P{^{1}H} NMR spectrum does not show the expected doublet and triplet pattern in a 2:1 ratio expected for an AX_2 spin system as found in **2**. The ^{31}P{^{1}H} NMR spectrum of **3**, shown in Figure 12a, is instead, a classical AB_2 second-order spin system, ignoring the couplings to ^{195}Pt, due to the small chemical shift difference between the two phosphorus resonances.[37]The simulated spectrum shown in Figure 12b was obtained by using the chemical shifts for P_A, 110.65 ppm, and P_B, 108.41 ppm. The ^{31}P−^{31}P coupling constant used for the simulation was $^3J(P_A,P_B) = 55.0$ Hz. The ^{1}H NMR spectrum of **3** shows only a single hydride resonance with coupling to both platinum and phosphorus, −7.42 ppm (m, ^1J(Pt,H) = 760 Hz, 4 H). This multiplet is a very complex second-order pattern due to the magnetic nonequivalence of the hydride ligands and was not simulated. The phosphorus decoupled ^{1}H NMR spectrum of **3** shows only a sharp singlet, except for the

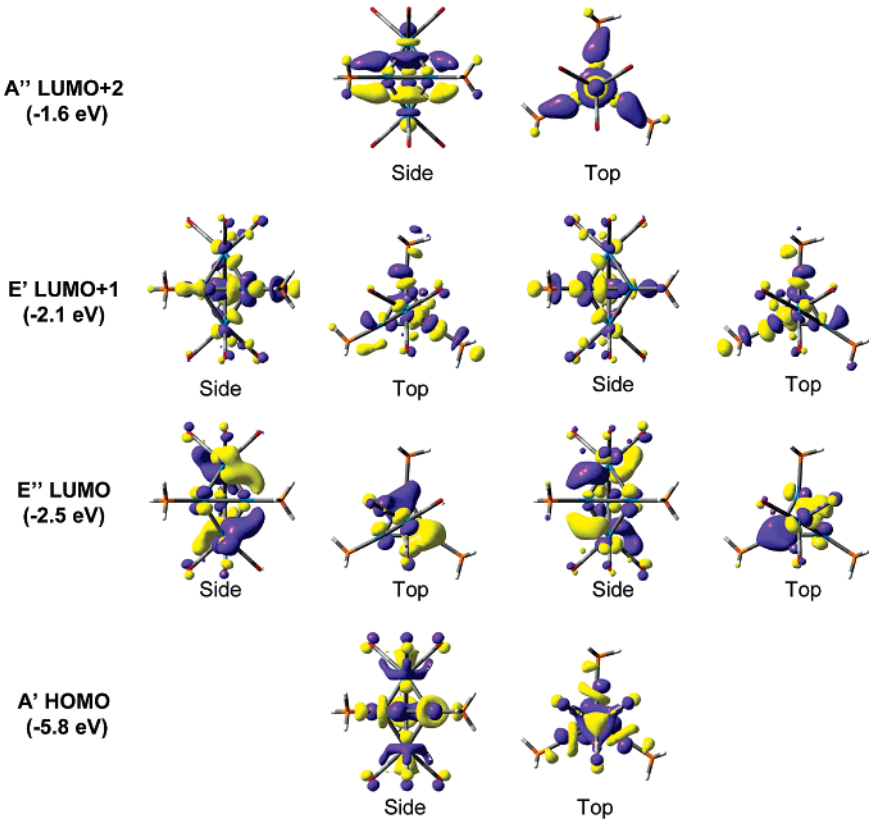

Figure 14. Side and top views of the A′ HOMO, the degenerate pairs of the E″ LUMO, the E′ LUMO + 1, and the A″ LUMO + 2 generated from a single-point B3PW91/BS1 calculation of $Re_2Pt_3(CO)_6(PH_3)_3$ with approximate D_{3h} symmetry of the non-hydrogen atoms (isovalue 0.04).

couplings to ^{195}Pt for the hydride resonance, indicating that the multiplet pattern of the central resonance is due to complex ^{31}P−^{1}H couplings.

The addition of D_2 to **1** is significantly slower than the addition of H_2. A KIE of approximately 1.3(1) for the formation of **2**-d_2 from **1** was determined by following the addition by IR spectroscopy. It appeared that similar isotopes effects were operative for the subsequent conversions of **2**-d_2 to **3**-d_4 and **3**-d_4 to **4**-d_6 by reactions with D_2 in the overall conversions, but these reactions were not measured separately.

The rate of addition of H_2 to **1** was also followed in a hexane solution containing a 20-fold excess of free PBu^t_3. The reaction was followed by IR spectroscopy of the CO absorptions of the four compounds. There was no discernible difference in the rates of formation of **2**−**4** in the presence or absence of the free PBu^t_3. This is interpreted as being consistent with an addition mechanism that does *not* involve the dissociation of a PBu^t_3 ligand prior to the addition of the hydrogen molecule. Examination of a space-filling model of **1** shows that there is probably enough space between the *tert*-butyl groups in the region above the Pt−Pt bonds in the plane of the Pt_3 triangle for a H_2 molecule to penetrate the ligand sphere and approach the metal atoms; see Figure 13.

Electronic Structure of 1. To understand the nature of the electronic unsaturation in **1**, we analyzed the molecular orbitals generated from B3PW91/BS1 calculations. To simplify the MO analysis, the QM model, $Re_2Pt_3(CO)_6(PH_3)$, was used as the model for **1**, and furthermore, the input structure for the single-point calculation was set up by basing the coordinates for the Re, Pt, P, C, and O atoms on the crystal coordinates and then adding the H atoms to generate the PH_3 fragments such that

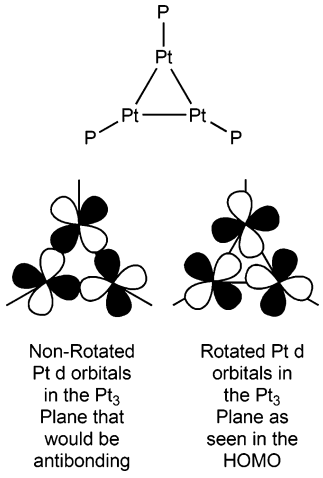

Figure 15. Schematic representation of the rotation of the platinum d orbitals that is observed in the B3PW91/BS1 HOMO of $Re_2Pt_3(CO)_6(PH_3)$, which decreases the Pt−Pt triangle edge antibonding character and increases the Pt−Pt−Pt bonding character in the center of the Pt_3 triangle. The two $Re(CO)_3$ units and hydrogen atoms of the PH_3 ligands are not shown.

the molecule had precise C_{3h} symmetry, while the non-hydrogen atoms had approximate D_{3h} symmetry. Similar to previously reported Fenske−Hall calculations,[16] the DFT molecular orbital analysis revealed the existence of five low-lying unoccupied molecular orbitals (LUMOs) in the form of a degenerate pair at −2.5 eV having E″ symmetry, the LUMO, a second degenerate pair, LUMO + 1, at −2.1 eV having E′ symmetry, and one nondegenerate orbital at −1.6 eV which has A_2'' symmetry; see Figure 14. These five orbitals could accommodate the anticipated 10 "missing" valence bonding electrons. The

Scheme 3. Proposed General Pathway for the Addition of 3 equiv of Dihydrogen to **1**

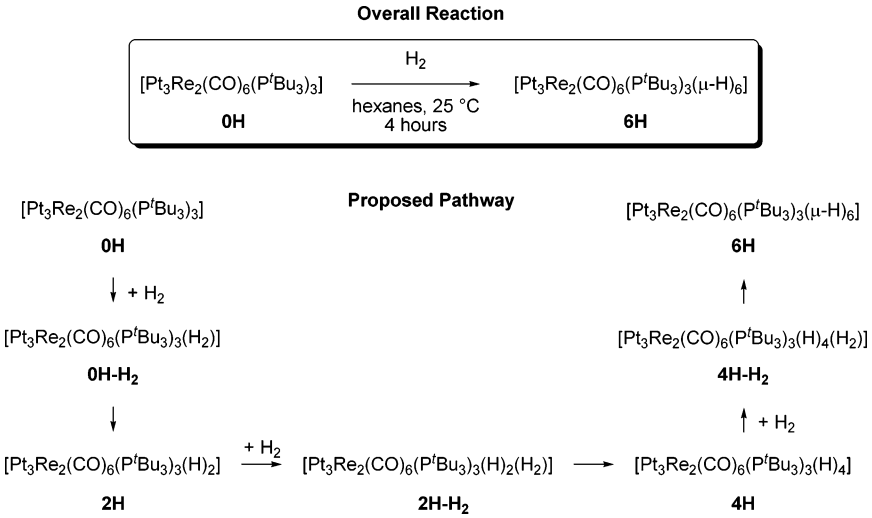

highest occupied molecular orbital (HOMO) of A_1' symmetry lies at −5.8 eV. This orbital is dominated by Pt−Pt interactions in the Pt_3 plane, and interestingly, the Pt d orbitals in the Pt_3 plane are "twisted" to generate a bonding region in the center of the Pt_3 triangle and to reduce the antibonding component of the orbital along the edges of the Pt−Pt triangle (Figures 14 and 15).

Calculated Structures of the 0H, 2H, 4H, and 6H Complexes with the QM and QM/MM Models. Three equivalents of dihydrogen can be added to the **1** cluster to generate **4**. IR analysis indicates that the addition of each molecule of dihydrogen occurs sequentially, and furthermore, the addition of 20 equiv of PBu^t_3 to the solution does not slow the reaction, which suggests that PBu^t_3 dissociation does not occur during the addition of dihydrogen. Thus, a plausible pathway for the addition of 3 equiv of dihydrogen to **1** involves three successive steps in which each equivalent of dihydrogen may coordinate to the cluster and is activated and converted into two hydride ligands (Scheme 3).

The positions of the hydrido ligands were located in the X-ray analysis of **4** (**6H**), and IR and NMR evidence suggests C_{2v} symmetry for the hydrido ligands in the dihydride **2** (**2H**) and the tetrahydride **3** (**4H**) complexes, but the positions of the hydrido ligands were not located in the X-ray analysis of **2** and **3** complexes, and there is no experimental information regarding the structures of potential dihydrogen intermediates (**0H-H_2**, **2H-H_2**, **4H-H_2**). Therefore, computational methods were used to investigate possible structures of the intermediates in this pathway, with the ultimate goal of providing an enhanced understanding of the process of hydrogen activation and storage on **1**.

Initially, the geometries and relative energies of the starting complex **1** (**0H**) and the overall product of the addition of 3 equiv of hydrogen **4** (**6H**) were optimized using a QM model, which employed the B3PW91/BS1 level of theory and a truncated model in which PH_3 was used in place of PBu^t_3, and a QM/MM model which employed the ONIOM(B3PW91/BS1:UFF) level of theory where the Bu^t groups were modeled with the UFF molecular mechanics level of theory. The initial geometries that were used as starting points for the geometry optimizations for the **0H** and **6H** complexes were based on the experimental X-ray structures, and the subsequent optimized geometries that resulted from using the QM and QM/MM models are similar to the X-ray structures and are presented in Figures 16 and 17.

Because the positions of the hydrido ligands were not located in the X-ray analysis of **2H** and **4H**, the structures and relative energies of a number of isomers that contained two and four hydrido ligands were calculated using the QM and QM/MM models to locate the preferential binding positions of the hydrido ligands.[38] The lowest energy isomers of the **2H** complex for both the QM and QM/MM models contained the two hydrido ligands in bridging positions along the two Re−Pt bonds from the same platinum atom. All other isomers of **2H** that were located that did not contain the two hydride ligands in bridging

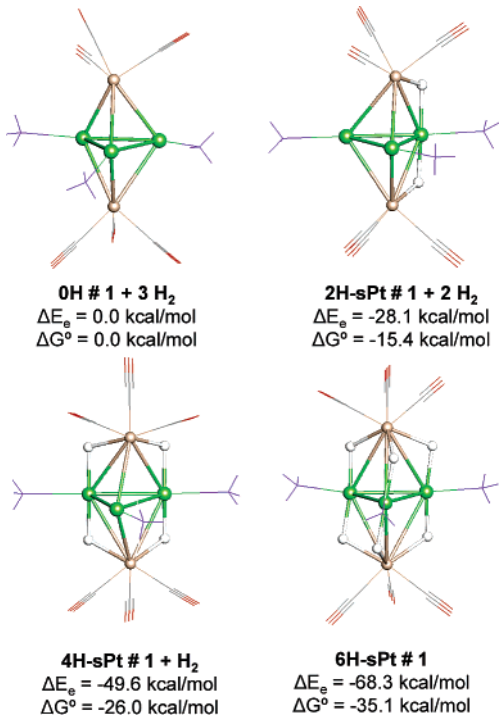

Figure 16. QM-model-optimized structures and relative energies of the **0H**, **2H**, **4H**, and **6H** complexes. The relative energies were compared to the energy of the lowest energy **0H** structure + $3H_2$, 0.0 kcal/mol. Key: platinum (green), rhenium (beige), phosphorus (purple), oxygen (red), carbon (gray), hydrogen (white).

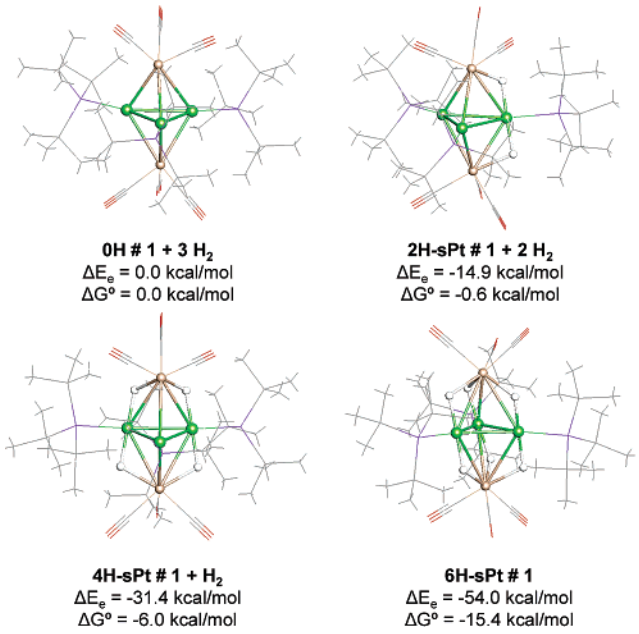

Figure 17. QM/MM-model-optimized structures and relative energies of the **0H**, **2H**, **4H**, and **6H** complexes. The relative energies were compared to the energy of the lowest energy **0H** structure + $3H_2$, 0.0 kcal/mol. Key: platinum (green), rhenium (beige), phosphorus (purple), oxygen (red), carbon (gray), hydrogen (white).

positions along the two Re−Pt bonds from the same platinum atom were higher in free energy by more than 12 and 16 kcal/mol for the QM and QM/MM models, respectively. Similarly, the lowest energy isomers of the **4H** complex for both the QM and QM/MM models contained all four of the hydrido ligands in bridging positions along Re−Pt bonds, with two hydrides attached to each of two Pt atoms (Figures 16 and 17). All other isomers of **4H** that were located that did not contain all four of the hydride ligands in bridging positions along Re−Pt bonds, with two hydrides attached to each of two Pt atoms, were higher in free energy by more than 10 and 22 kcal/mol for the QM and QM/MM models, respectively. The QM and QM/MM structures of the lowest free energy **2H** and **4H** isomers are consistent with the NMR experiments which indicate that the **2H** and **4H** complexes display approximate C_{2v} symmetry in solution.

The lowest relative energy structures of the **0H**, **2H**, **4H**, and **6H** complexes that were optimized using the QM model and the QM/MM model are presented in Figures 16 and 17, respectively. For the QM model (Figure 16), the addition of each equivalent of H_2 to the bimetallic Re_2Pt_3 cluster is exergonic, such that compared to that of **0H#1** + $3H_2$, the relative gas-phase free energies of **2H-sPt#1** + $2H_2$, **4H-sPt#1** + H_2, and **6H-sPt#1** are −15.4, −26.0, and −35.1 kcal/mol, respectively. For the QM/MM model (Figure 17), the addition of each equivalent is also exergonic, such that compared to that of **0H#1** + $3H_2$, the relative gas-phase free energies of **2H-sPt#1** + $2H_2$, **4H-sPt#1** + H_2, and **6H-sPt#1** are −0.6, −6.0, and −15.4 kcal/mol, respectively. The calculated relative free energies for both the QM and QM/MM models are consistent with the experimental observations that compounds **2** (**2H**), **3** (**4H**), and **4** (**6H**) are readily formed upon the reaction of **1** (**0H**) with excess H_2.

(38) Details of the search for alternative isomers of the **2H** and **4H** complexes are provided in the Supporting Information.

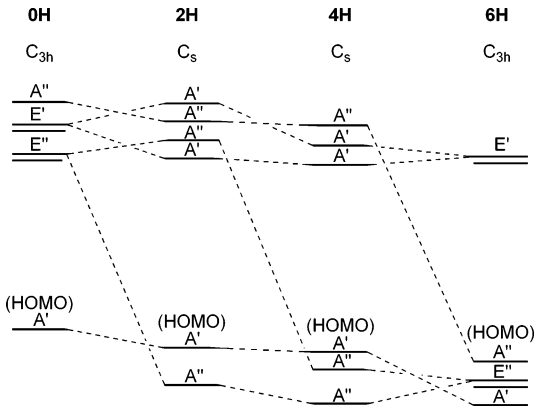

Figure 18. Correlation energy diagram for the **0H**, **2H**, **4H**, and **6H** complexes.

Correlation Energy Diagram. With the information regarding the preferred locations of the hydride ligands in the **2H** and **4H** complexes in hand, we sought to identify the frontier orbitals that are affected upon each addition of dihydrogen to the cluster of **1**. For this molecular orbital analysis, the smaller QM model was used, and to simplify further the analysis of the molecular orbitals, the **6H** complex was constrained to C_{3h} symmetry and the **2H** and **4H** complexes were constrained to C_s symmetry. The **2H**, **4H**, and **6H** complexes were then optimized with the symmetry constraints, and the resulting B3PW91/BS1 orbitals were examined (Figure 18). The orbitals for the **0H** complex used in the analysis were obtained as described previously (vide supra).

Upon addition of the first equivalent of dihydrogen, the E″ and E′ orbitals are split due to the reduction of symmetry. The two added electrons are added to one of the orbitals, A″, derived from the E″ set. The electrons from the addition of the second equivalent of dihydrogen to form **4H** are added to the second A″ orbital from the original E″ set and complete the filling of that set. Subsequently, the third equivalent of dihydrogen provides two electrons which fill another A″ orbital from **4H**, so that **6H** contains filled E″ and A″ orbitals that were originally unoccupied in **0H** (Figure 18). Notably, the **0H** E″ and A″ orbitals that become filled upon the addition of the 3 equiv of H_2 have bonding character along Re−Pt edges, while the **0H** E′ orbitals, which remain unoccupied throughout this series of complexes, do not have bonding character along the Re−Pt bonds (Figure 14).

Computational Investigation of H_2 Addition and Binding. Another aspect of the reactivity of these RePt cluster complexes toward dihydrogen that we sought to explain by using the QM and QM/MM computational models was the nature of the addition and coordination of H_2 to **0H**, **2H**, and **4H** to generate the **0H-H_2**, **2H-H_2**, and **4H-H_2** complexes, respectively, that might represent intermediates in the hydrogen activation reactions.

With the QM model, optimized structures were located for H_2 binding to both Pt and Re atoms in the **0H** and **2H** complexes, producing **0H-H_2** and **2H-H_2** structures, while for the **4H** complex, an optimized structure, **4H-H_2**, was only located for H_2 binding to Re. In terms of free energy, H_2 binding to the **0H**, **2H**, and **4H** complexes to generate the **0H-H_2**, **2H-H_2**, and **4H-H_2** complexes is endoergic in all cases (Figures 19 and 20 and Figures S2−S4 in the Supporting Information). In

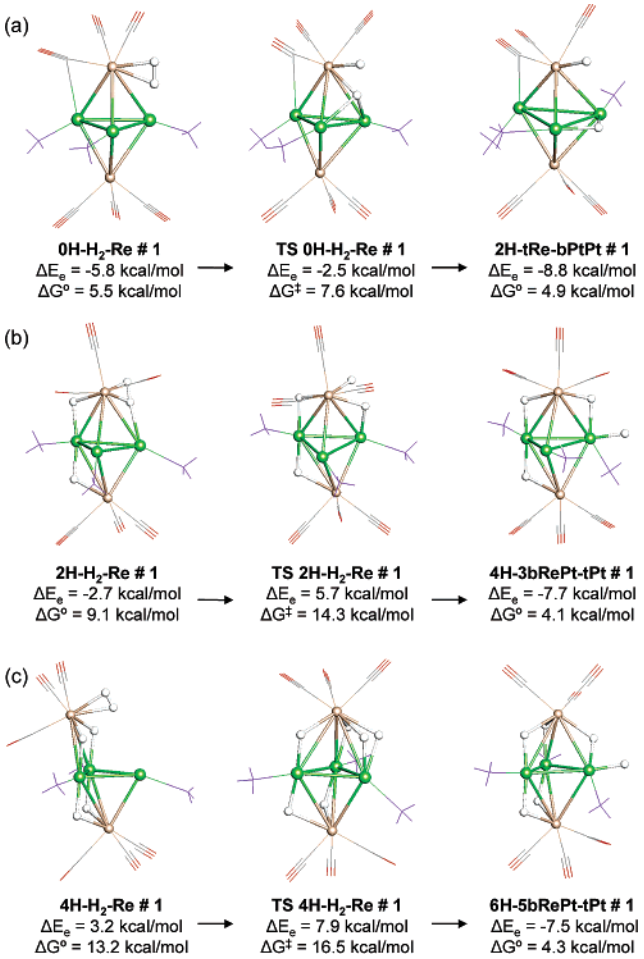

Figure 19. QM-optimized dihydrogen complexes, transition states for H_2 activation, and resulting local minima for the **0H-H$_2$-Re** (a), **2H-H$_2$-Re** (b), and **4H-H$_2$-Re** (c) series of complexes. Relative energies of the **0H-H$_2$-Re** series (a) are compared to the energy of the lowest energy **0H** complex + H_2, 0.0 kcal/mol. Relative energies of the **2H-H$_2$-Re** series (b) are compared to the energy of the lowest energy **2H** complex + H_2, 0.0 kcal/mol. Relative energies of the **4H-H$_2$-Re** series (c) are compared to the energy of the lowest energy **4H** complex + H_2, 0.0 kcal/mol. Key: platinum (green), rhenium (beige), phosphorus (purple), oxygen (red), carbon (gray), hydrogen (white).

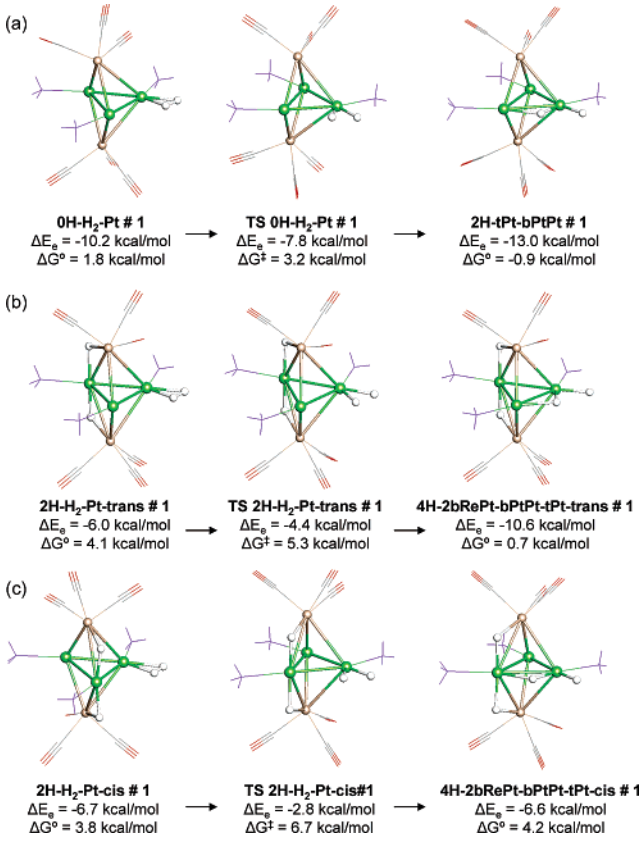

Figure 20. QM-optimized dihydrogen complexes, transition states for H_2 activation, and resulting local minima for the **0H-H$_2$-Pt** (a), **2H-H$_2$-Pt-*trans*** (b), and **2H-H$_2$-Pt-*cis*** (c) series of complexes. Relative energies of the **0H-H$_2$-Pt** series (a) are compared to the energy of the lowest energy **0H** complex + H_2, 0.0 kcal/mol. Relative energies of the **2H-H$_2$-Pt-*trans*** (b) and **2H-H$_2$-Pt-*cis*** (c) series are compared to the energy of the lowest energy **2H** complex + H_2, 0.0 kcal/mol. Key: platinum (green), rhenium (beige), phosphorus (purple), oxygen (red), carbon (gray), hydrogen (white).

these complexes H_2 binds to Pt more strongly than to Re (compare the first columns of Figures 19 and 20). In spite of the result that H_2 binding to the Pt atoms generates more stable complexes, repeated attempts to locate a **4H-H$_2$** complex in which H_2 was bound to Pt failed.

With the QM/MM model, optimized structures were located for **0H-H$_2$**, **2H-H$_2$**, and **4H-H$_2$** complexes in which H_2 is bound to a Re atom (see Figure 21 and Figures S5−S7 in the Supporting Information). Including the steric bulk of the Bu^t groups further disfavors H_2 binding by 19, 14, and 7 kcal/mol for **0H**, **2H**, and **4H**, respectively (compare the first columns of Figures 19 and 21). Despite repeated attempts, freely optimized structures in which H_2 was bound to the Pt were not located for the QM/MM model. Relaxed potential energy scans with loosened convergence criteria indicated that the electronic energy increased as the H_2−Pt distance was decreased. This suggests that **0H-H$_2$**, **2H-H$_2$**, and **4H-H$_2$** complexes in which the H_2 is closely bound to the Pt either are not local minima or are very shallow local minima on the QM/MM potential energy surface.

In the process of binding H_2 to the **0H** and **2H** complexes to generate the corresponding **0H-H$_2$** and **2H-H$_2$** complexes, with both the QM and QM/MM models, the trigonal bipyramidal structure of the core Re_2Pt_3 unit generally remains intact. However, with the QM model for H_2 binding to the Re atom of the **4H** complex that generates **4H-H$_2$-Re#1** (Figure 19c), the trigonal bipyramidal structure of the Re_2Pt_3 is significantly distorted such that the complex has opened to facilitate H_2 binding. In the QM/MM model of the **4H-H$_2$-Re#1** complex (Figure 21c), there is less distortion of the Re_2Pt_3 from the trigonal bipyramidal structure, which is likely because the steric bulk of the *tert*-butyl group blocks the opening of the top of the Re_2Pt_3 to the extent observed with the smaller QM model.

Computational Investigation of H$_2$ Activation. In addition to locating the structures of the H_2 adducts that were described above, transition states were located for dihydrogen activation (cleavage) from the **XH-H$_2$-Re** complexes for both the QM model (center column, Figure 19) and QM/MM model (center column, Figure 21). With the QM model, the free energies for cleavage are 2.1, 5.2, and 3.3 kcal/mol higher than the energies of the preceding dihydrogen complexes for the **0H**, **2H**, and **4H** systems, respectively. Although the free energies of the products of the cleavage (last column, Figure 19) are below the TS free energies, these products are still higher in free energy than the reactant cluster + H_2 (the energy reference).

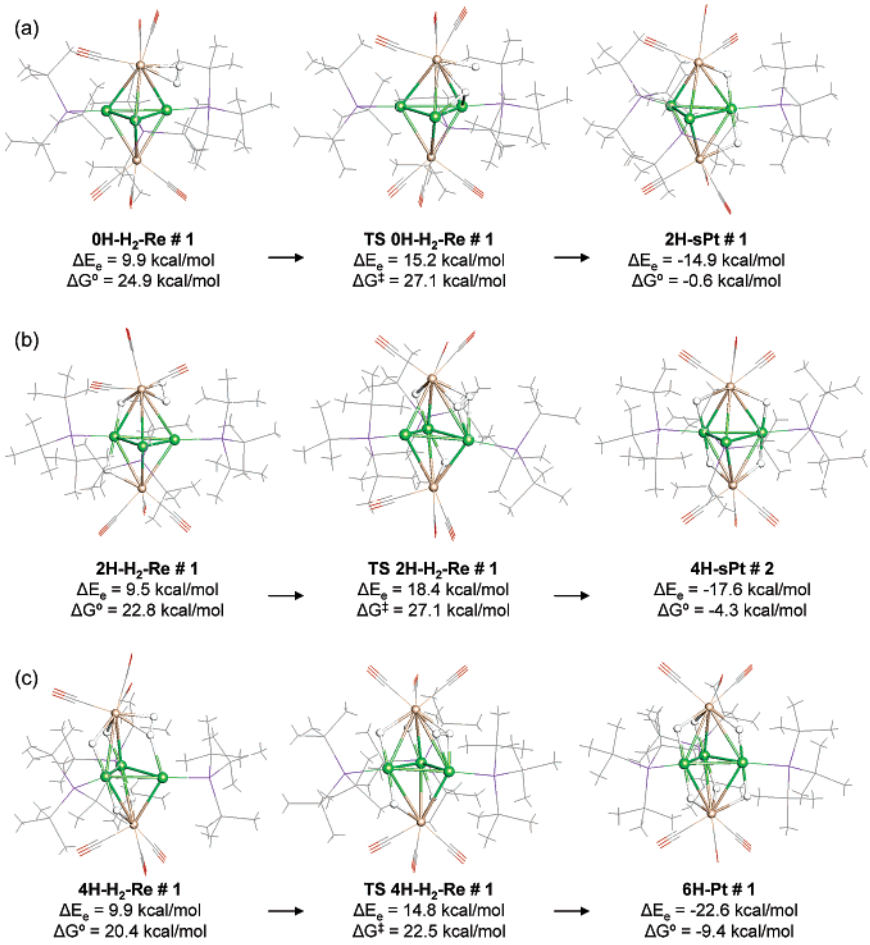

Figure 21. QM/MM-optimized dihydrogen complexes, transition states for H_2 activation, and resulting local minima in the **0H-H_2-Re** (a), **2H-H_2-Re** (b), and **4H-H_2-Re** (c) series of complexes. Relative energies of the **0H-H_2-Re** series (a) are compared to the energy of the lowest energy **0H** complex + H_2, 0.0 kcal/mol. Relative energies of the **2H-H_2-Re** series (b) are compared to the energy of the lowest energy **2H** complex + H_2, 0.0 kcal/mol. Relative energies of the **4H-H_2-Re** series (c) are compared to the energy of the lowest energy **4H** complex + H_2, 0.0 kcal/mol. Key: platinum (green), rhenium (beige), phosphorus (purple), oxygen (red), carbon (gray), hydrogen (white).

In spite of the larger steric bulk in the QM/MM model, the hydrogen activation barriers are 2.2, 4.3, and 2.1 kcal/mol, respectively, like those in the smaller model. Now, however, the product of H_2 cleavage (last column, Figure 21) shows products that are much more stable than the **XH-H_2-Re** and even lower in free energy than the separated reactants.

A comparison of the hydrogen activation steps from the **XH−Re** complexes + H_2 that were obtained with the QM and QM/MM models reveals that the higher barriers in the more sterically crowded (experimental) system arise primarily because the binding of dihydrogen is much more endoergic in the QM/MM model than in the QM model. For both the QM and QM/MM models, in all cases the transition states are between 2 and 6 kcal/mol higher in free energy than the corresponding dihydrogen complexes, which indicates that hydrogen activation should occur readily after dihydrogen reaches Re centers in the **0H**, **2H**, and **4H** complexes. In another notable difference, the hydrogen activation steps calculated using the QM model for the **0H-H_2-Re**, **2H-H_2-Re**, and **4H-H_2-Re** complexes generate local minima as products in which both resulting hydride ligands are not bridging Re−Pt bonds, whereas for the QM/MM model of the corresponding complexes, analogous local minima were not located. Instead, optimization of input structures that are slightly on the product side of the QM/MM transition states yielded minima in which both resultant hydride ligands were bridging Re−Pt bonds. Thus, it appears that including the PBu^t_3 ligands through the use of the QM/MM model precludes the formation of some shallow local minima that are observed on the potential energy surface of the smaller QM model. These results suggest that, in the experimental system, once the dihydrogen enters the cluster, it is cleaved and the H atoms readily migrate to the RePt edges, the lowest energy positions.

For the small QM model, low-energy transition states for hydrogen activation at Pt were also located (Figure 20), and the resulting products all contain one hydride ligand that bridges a Pt−Pt bond and another hydride ligand that is in a terminal position on a Pt atom.

The analogous H_2−Pt complexes and transition states for dihydrogen activation on Pt could not be found for the larger QM/MM model. However, QM/MM structures analogous to the QM model local minima with H terminal and bridging Pt were located and optimized (Figure 22). Although it is probable that any QM/MM hydrogen activation transition states in which

(39) Efremenko, I. *J. Mol. Catal. A* **2001**, *173*, 19−59.
(40) (a) Moc, J.; Musaev, D. G.; Morokuma, K. *J. Phys. Chem. A* **2000**, *104*, 11606−11614. (b) Efremenko, I.; German, E. D.; Sheintuch, M. *J. Phys. Chem. A* **2000**, *104*, 8089−8096. (c) Wang, Y.; Cao, Z.; Zhang, Q. *Chem. Phys. Lett.* **2003**, *376*, 96−102.

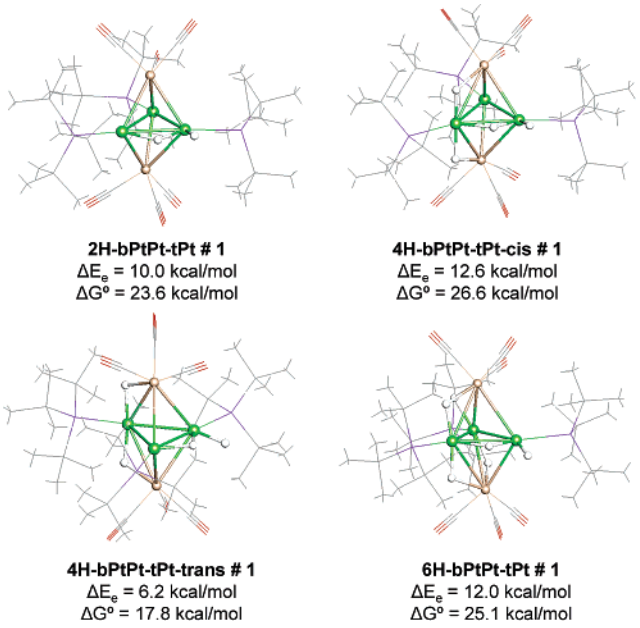

Figure 22. QM/MM-optimized structures of **2H**, **4H**, and **6H** complexes that contain a terminal hydride ligand attached to a Pt atom and another hydride ligand that bridges a Pt−Pt bond. The relative energy of **2H-bPtPt-tPt#1** is compared to the energy of the lowest energy **0H** complex + H_2, 0.0 kcal/mol. Relative energies of **4H-bPtPt-tPt-*cis*#1** and **4H-bPtPt-tPt-*trans*#1** are compared to the energy of the lowest energy **2H** complex + H_2, 0.0 kcal/mol. The relative energy of **6H-bPtPt-tPt#1** is compared to the energy of the lowest energy **4H** complex + H_2, 0.0 kcal/mol. Key: platinum (green), rhenium (beige), phosphorus (purple), oxygen (red), carbon (gray), hydrogen (white).

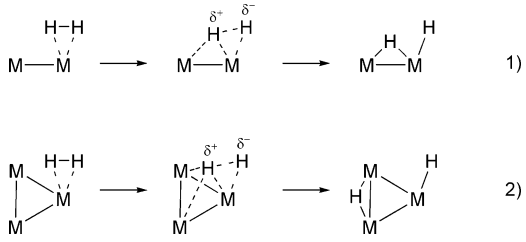

Figure 23. Schematic representation of the two-center (1) and three-center (2) activation of dihydrogen observed in the transition states **TS 0H-H$_2$-Pt#1** and **TS 0H-H$_2$-Re#1**.

hydrogen activation occurs in the Pt_3 plane would be higher in free energy than the metastable hydride product complexes shown in Figure 22, it is possible that there are transition states which lead to these complexes and that these transition states might not be much higher in free energy than the products, as in the QM model. Thus, it is possible that hydrogen addition in these Re_2Pt_3 clusters could be occurring through multiple hydrogen activation pathways.

It is worth noting that, in the hydrogen activation transition states that were located by using the QM and QM/MM models, the cleavage of the H−H bond often involves more than one metal atom. For example, two Pt atoms participate in the heterolytic dihydrogen cleavage in the QM model transition state **TS 0H-H$_2$-Pt#1** (Figure 20), and two Pt atoms and one Re atom participate in the heterolytic dihydrogen cleavage in the QM and QM/MM model transition states **TS 0H-H$_2$-Re#1** (Figures 19 and 21, respectively). Figure 23 shows a schematic representation of hydrogen cleavage mediated through multiple metal atoms. Activation pathways such as these may have implications

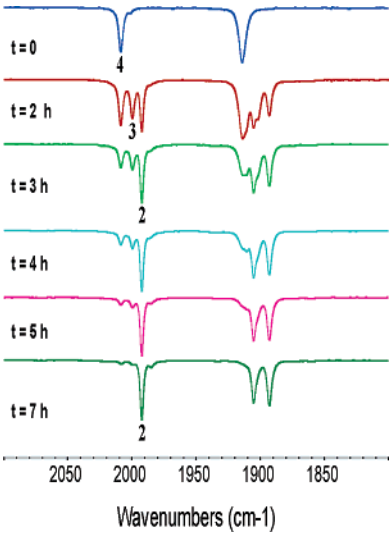

Figure 24. IR spectra in the CO absorption region showing the progressive transformation of **4** to **3** and then **2** as a function of time under the influence of UV−vis irradiation. Reaction times *t* in hours are shown on the left.

for the nature of hydrogen activation on metal surfaces[39] and have been invoked in multicenter activations of hydrogen on small ligand-free clusters.[40] Here, our results suggest that the $Re_2Pt_3(CO)_6(PBu^t_3)_3$ cluster system is able to add dihydrogen without ligand dissociation or without the presence of an obvious "vacant site" by utilizing these multiple metal atom hydrogen activation pathways. Recent computational studies of the complex $[Rh_6(PR_3)_6H_{16}][BAr^F_4]_2$ have indicated the existence of bridging H_2 coordination for some of the dihydrogen ligands in this complex.[4a]

Elimination of Hydrogen from 4. Efforts were made to induce the elimination of the hydrido ligands of **4** in the form of hydrogen. There was no evidence for elimination of the hydrido ligands even when **4** was heated to 175 °C. However, under the influence of UV−vis irradiation at room temperature, a solution of **4** in a Pyrex reaction flask was slowly converted back to **3** and then **2** over a period of hours. Stacked plots of these spectra as a function of time are shown in Figure 24. There was very little formation of compound **1** under these conditions. Spectroscopically, the conversion to **2** appears to be very high after 7 h, but because of the instability of this compound, it was possible to isolate it in pure form in only 27% yield. However, this is the best method to obtain **2** in a pure form. When irradiation of **4** was performed in a quartz reaction vessel, it was possible to observe the formation of small amounts of **1**, but the yield was very low, and most of the compounds decomposed under these conditions. We do not know why the photoelimination of hydrogen from **2** is so ineffective. We can only speculate that photoelimination of hydrogen from **2** is more difficult than the photoelimination of hydrogen from **3** and **4** and the radiation that passes through the Pyrex glassware is not sufficiently energetic to produce the hydrogen elimination from **2**. When a sample of **4** was irradiated similarly in a 10 mm NMR tube in toluene-d_8 solvent, it was possible to observe the formation of hydrogen in the ^{1}H NMR spectrum from its characteristic resonance at $\delta = 4.51$ ppm.

Acknowledgment. This research was supported by the Office of Basic Energy Sciences of the U.S. Department of Energy

under Grant No. DE-FG02-00ER14980. We thank Strem for donation of a sample of $Pt(PBu^t_3)_2$ and Johnson Matthey for a donation of K_2PtCl_4. The work at Texas A&M University was supported by the NSF (Grants CHE 0518074 and DMS 0216275), The Welch Foundation (Grant A-0648), and Texas A&M University. We thank Dr. Perry J. Pellechia for assistance with the NMR spectra and Dr. Mark D. Smith for collecting low-temperature X-ray diffraction data.

Supporting Information Available: Experimental data and CIF files for each of the structural analyses, additional optimized structures of dihydrogen adducts and other isomers of the **2H** and **4H** complexes, and an example of a Gaussian 03 input file used for the QM/MM calculations. This material is available free of charge via the Internet at http://pubs.acs.org.

JA067028G